The Sudbury Neutrino Observatory

Nick Jelley,[1] Arthur B. McDonald,[2] and R.G. Hamish Robertson[3]

[1]Department of Physics, Oxford University, Oxford OX1 3QR, United Kingdom; email: n.jelley@physics.ox.ac.uk

[2]Department of Physics, Queen's University, Kingston, Ontario K7L 3N6, Canada; email: art@snolab.ca

[3]Department of Physics and Center for Experimental Nuclear Physics and Astrophysics, University of Washington, Seattle, Washington 98195; email: rghr@u.washington.edu

Annu. Rev. Nucl. Part. Sci. 2009. 59:431–65

The *Annual Review of Nuclear and Particle Science* is online at nucl.annualreviews.org

This article's doi: 10.1146/annurev.nucl.55.090704.151550

0163-8998/09/1123-0431$20.00

Key Words

solar neutrino, neutrino oscillation, heavy water, Cherenkov detector

Abstract

The solar neutrino problem arose when the first measurements of the flux of neutrinos from the Sun, taken by Raymond Davis, Jr. with a Cl-Ar radiochemical detector, fell substantially below the value predicted theoretically by John Bahcall. Bahcall's prediction came from a detailed model of the nuclear reactions powering the Sun. Resolution of the problem came three decades later with the observation of nonelectron flavors of neutrinos in the solar flux. The use of heavy water in the Sudbury Neutrino Observatory (SNO) experiment provided a means to measure both electron and nonelectron components, and the presence of the latter showed that neutrino flavor conversion was taking place—a hallmark of neutrino oscillation and mass. The solar models were vindicated, and the Standard Model of elementary particles and fields had to be revised. Here we present an account of the SNO project, its conclusions to date, and its ongoing analysis.

Contents

1. INTRODUCTION

The Sudbury Neutrino Observatory (SNO) was designed to make a definitive measurement of solar neutrinos, clearly determining whether they change from one type to another, by using heavy water as a target. This measurement was motivated by the measurements taken by Davis and coworkers (1), which indicated that fluxes of electron neutrinos from the Sun were lower than had been calculated by the comprehensive solar models (2) developed by Bahcall and others (3). This discrepancy had come to be known as the solar neutrino problem. The advantages of using heavy water in this measurement were described in a seminal paper by Herbert Chen (4). Chen and George Ewan acted as cospokesmen for the SNO collaboration after it was founded in 1984.

Deuterium provides the opportunity to observe two reactions for solar neutrinos: the charged-current (CC) reaction, which is specific to electron neutrinos at solar neutrino energies, and the

neutral-current (NC) reaction, which is equally sensitive to all active neutrino types. By comparing the fluxes observed by these two reactions, it is possible to determine (*a*) whether electron neutrinos produced by one of the nuclear reactions powering the Sun change to other active types in transit to the Earth and (*b*) the total flux of these neutrinos to compare with solar model calculations.

To make these measurements, the SNO collaboration built an ultraclean detector containing 1000 tonnes[1] of heavy water (valued at ~$300 million), 2 km underground in an active nickel mine, and spent a number of years making observations. This article is the story of this experiment and of how it showed that electron neutrinos from the core of the Sun change to other types of neutrino, requiring extensions to the Standard Model of elementary particles and confirming that solar models are accurate.

This article describes the extensive work that went into the experiment, ranging from the initial design, to a complex construction period, to the commissioning, operation, and removal of the heavy water, and summarizes the analysis of the data. It is the story of a massive experimental adventure, involving more than 500 people over 24 years, that followed from an inspired idea of Herb Chen. whose life was tragically ended by leukemia in 1987 before construction started in 1990.

2. THE SOLAR NEUTRINO PROBLEM

Solar neutrinos allow the direct study of the nuclear fusion reactions in the Sun that convert hydrogen to helium with the release of energy via a series of reactions, summarized by

$$4p + 2e^- \rightarrow {}^4\mathrm{H}e + 2\nu_e + 26.731\,\mathrm{MeV}.$$

The primary process of conversion in the Sun is the *pp* chain of reactions that produces 98% of all the energy; the CNO cycle contributes only 2%. The neutrino energy spectrum from the *pp* chain is shown in **Figure 1** (5).

The first experiment to observe solar neutrinos was carried out by Davis's group from Brookhaven National Laboratory (7). The group used 615 tons of the dry-cleaning fluid perchloroethylene (C_2Cl_4), which was located in a laboratory in the Homestake gold mine, to detect the inverse beta-decay reaction

$$\nu_e + {}^{37}\mathrm{Cl} \rightarrow {}^{37}\mathrm{Ar} + e^- - 0.814\,\mathrm{MeV}.$$

The Q-value of the reaction is such that the experiment was sensitive to ^{7}Be, CNO, and, predominantly, the weak ^{8}B branch in the *pp* chain. A rate of approximately 2 events per day was expected, and the first result published in 1968 (7) reported a limit ~2.5 times smaller than predicted.

Although the total number of solar neutrinos is strongly constrained by the Sun's luminosity, the relative neutrino fluxes in the *pp* chain are not; in particular, the competition between $^3\mathrm{He} + {}^3\mathrm{He} \rightarrow {}^4\mathrm{He} + 2p$ and $^3\mathrm{He} + {}^4\mathrm{He} \rightarrow {}^7\mathrm{Be} + \gamma$ and between $e^- + {}^7\mathrm{Be} \rightarrow {}^7\mathrm{Li} + \nu_e$ and $p + {}^7\mathrm{Be} \rightarrow {}^8\mathrm{B} + \gamma$ determines the energy spectrum of the neutrinos shown in **Figure 1**. The calculation of these fluxes requires a detailed solar model, and at the time the prediction of the ^{8}B flux was made (1968), Bahcall felt that the theoretical uncertainty was sufficient to contradict the idea that the observed deficit meant "that something fundamental was really wrong" (8).

[1]One tonne is equivalent to 1000 kg.

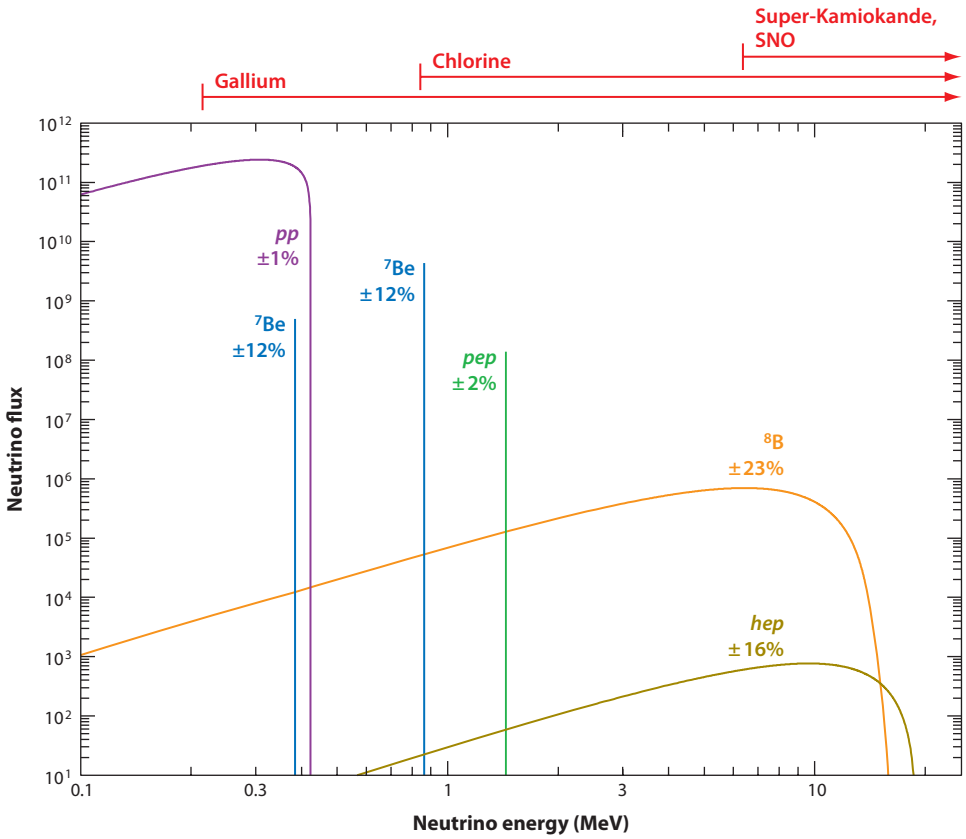

Figure 1

Energy spectra of neutrinos from the *pp* chain predicted by the Standard Solar Model (6). The neutrino fluxes from continuum sources (*pp* and ^{8}B) are given in cm^{-2} s^{-1} MeV^{-1} at 1 AU. The line fluxes (*pep* and ^{7}Be) are given in cm^{-2} s^{-1}. The red arrows at the top represent the thresholds of the indicated experiments. The higher-energy ^{7}Be line is just above threshold in the chlorine experiment. CNO neutrinos are omitted for simplicity. Reproduced from Reference 5 with permission from IOP Publishing, Ltd. and Deutsche Physikalische Gesellschaft.

Over the next decade, both the experiment and the theoretical calculation were refined. By 1978, solar neutrinos had been definitely detected (1), but the flux was still about 2.5 times lower than the predicted flux (9). Between 1968 and 1978, many effects that might reduce the central temperature of the Sun and hence the ^{8}B solar neutrino flux had been considered. One of the more reasonable effects was that the interior of the Sun was essentially devoid of heavy elements. Also, researchers extensively examined the nuclear cross-section measurements relevant to the *pp* chain, but no explanation for the discrepancy was apparent. The lack of agreement is what became known as the solar neutrino problem.

In 1990, the Kamiokande-II 2140-tonne water Cherenkov detector experiment reported (10) that the flux of ^{8}B solar neutrinos, deduced from the number of ν_e-electron elastic scattering (ES) events above a threshold energy of 7.5 MeV, was 0.44 $\pm$ 0.06 that of the Standard Solar Model (SSM) (11). This result confirmed the deficit of solar neutrinos observed by the Homestake experiment and also showed that the neutrinos came from the Sun. However, comparing the rates

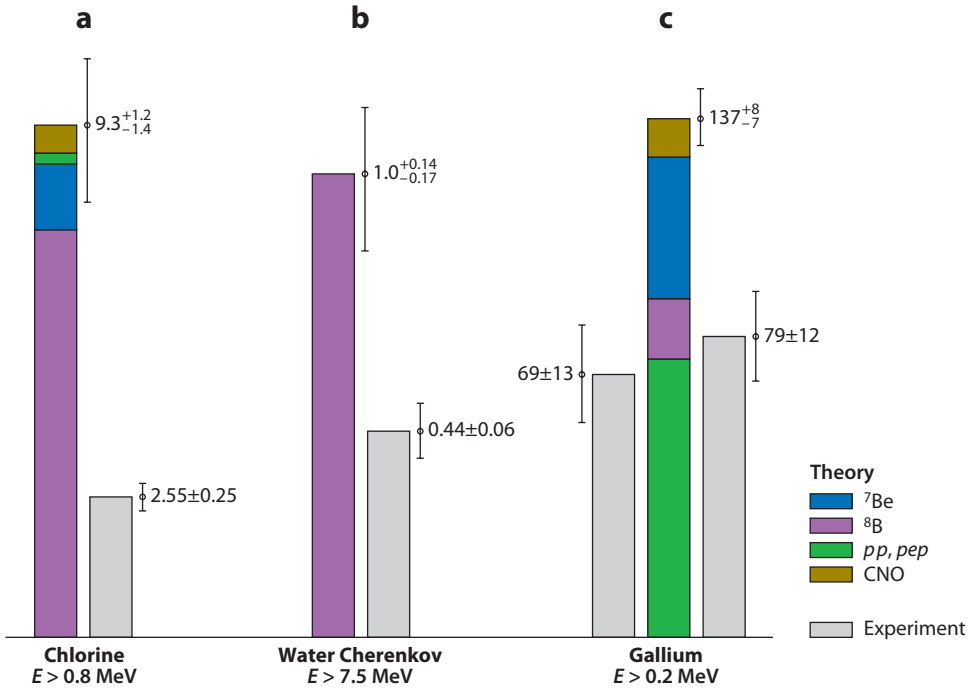

Figure 2

Comparison of the measured rates with the Standard Solar Model predictions for the (*a*) chlorine, (*b*) water Cherenkov, and (*c*) gallium solar neutrino experiments. Reproduced from Reference 11 with permission from the AAS.

of the water Cherenkov and chlorine experiments implied a negative contribution from the *pep*, CNO, and ^{7}Be neutrinos to the chlorine experiment. Bahcall termed this apparent incompatibility the second solar neutrino problem (11).

In the early 1990s, further experimental confirmation of a deficit in solar neutrinos came with the results from the gallium experiments, SAGE (12) and GALLEX (13), that detected the neutrinos from the initial *pp* chain reaction through the reaction

$$\nu_e + {}^{71}\mathrm{Ga} \rightarrow {}^{71}\mathrm{Ge} + e^- - 0.233\,\mathrm{MeV}.$$

The results from the two gallium experiments and from the water Cherenkov and chlorine experiments are shown in **Figure 2**. The mean value of the solar neutrino flux from the gallium experiments is very close to the flux of *pp* and *pep* neutrinos. It also leaves no room for the contribution from ^{7}Be neutrinos, an effect termed the third solar neutrino problem (11).

By 1996, there was growing evidence that these problems did not originate with solar models: Even when the fluxes were treated as arbitrary parameters, there was no consistent solution (14, 15). Further confirmation emerged with the excellent agreement found between the predictions of solar models and data for helioseismological data on *p*-mode oscillations that sampled deep into the interior of the Sun (8). The fractional difference averaged less than 0.1% in the interior when new opacity data and, in particular, helium and heavy element diffusion were included in the SSM. These experimental and theoretical investigations strongly suggested that the answer to the solar neutrino problem(s) lay in the physics of neutrinos.

3. PARTICLE PHYSICS SOLUTIONS

The idea that the solar neutrino problem might be caused by neutrino oscillations dates to a suggestion made by Pontecorvo in 1967 (16, 17). Originally conceived as $\nu_e \rightarrow \bar{\nu}_e$, the term neutrino oscillations now refers to the flavor evolution in space or time of a neutrino state initially prepared in a pure flavor, such as the pure electron flavor that solar fusion reactions produce. Because the Cl-Ar experiment was sensitive only to electron flavor neutrinos, oscillation to another flavor would render the neutrinos invisible. At that time, only the electron and muon neutrinos were known; the third flavor of lepton, tau, was not discovered until 1975 (18). There is nothing in the Standard Model that prohibits neutrinos from being states of mixed flavor: The same phenomenon occurs in quarks. However, for any evolution to occur, neutrinos must also have mass, whereas in the Standard Model they are massless. Evolution of flavor follows when neutrinos with definite mass are not eigenstates of flavor and vice versa. The two representations are related through a unitary transformation matrix $\mathbf{U}_{\mathrm{MNSP}}$, the Maki–Nakagawa–Sakata–Pontecorvo matrix (19):

$$\begin{pmatrix} \nu_e \\ \nu_\mu \\ \nu_\tau \end{pmatrix} = \begin{pmatrix} U_{e1} & U_{e2} & U_{e3} \\ U_{\mu 1} & U_{\mu 2} & U_{\mu 3} \\ U_{\tau 1} & U_{\tau 2} & U_{\tau 3} \end{pmatrix} \begin{pmatrix} \nu_1 \\ \nu_2 \\ \nu_3 \end{pmatrix}.$$

The nine elements of the matrix are not all independent. A standard way to recast $\mathbf{U}_{\mathrm{MNSP}}$ is in terms of three mixing angles, θ_{12}, θ_{13}, and θ_{23}, and either one or three phases, depending on whether neutrinos and antineutrinos are different or identical (20). These phases do not affect solar neutrino oscillations.

The electron neutrino is given in terms of the mass eigenstates by

$$\nu_e = U_{e1}\nu_1 + U_{e2}\nu_2 + U_{e3}\nu_3.$$

If the masses of ν_i are zero, this relationship between mass and flavor eigenstates stays the same at all times and positions. However, if the masses are nonzero, then

$$\nu_e(t) = U_{e1}e^{-iE_1 t}\nu_1 + U_{e2}e^{-iE_2 t}\nu_2 + U_{e3}e^{-iE_3 t}\nu_3,$$

where $E_i^2 = p^2 + m_i^2$ and where the state evolves with time or distance. The overall phase is unobservable:

$$\nu_e(t) = e^{-iE_1 t}(U_{e1}\nu_1 + U_{e2}e^{-i(E_2-E_1)t}\nu_2 + \cdots).$$

When $m_i^2 \ll p^2$, then $E_j - E_i = \frac{(m_j^2 - m_i^2)L}{2E}$, and observable effects depend on mass-squared differences, neutrino energy, distance, and the matrix elements U_{ei}. For negligibly small θ_{13}, the electron neutrino survival probability in vacuum is

$$P_{ee} = 1 - \sin^2 2\theta_{12} \sin^2\left(\frac{1.27\Delta m_{12}^2 L}{E}\right),$$

where $\Delta m_{12}^2 = m_2^2 - m_1^2$ is measured in electronvolts squared, E is the energy in megaelectronvolts, and L is the distance in meters.

Wolfenstein noted in 1978 (21) that in the presence of matter with N scatterers per unit volume, the forward scattering amplitude $f_l(0)$ leads to a neutrino refractive index,

$$n_l = 1 + \frac{2\pi N}{p^2} f_l(0),$$

that is different for the electron flavor than for the other two flavors because of W exchange, which can occur only for electron neutrinos interacting with electrons. Then,

$$n_e = 1 + \frac{2\pi N_e}{p^2}\left(\sqrt{2}\frac{G_F p}{2\pi} + \mathrm{NC}\right),$$

where G_F is the Fermi constant and where the flavor-independent part is indicated by NC (22). For 10-MeV neutrinos, even at the center of the Sun (density ~156 g cm^{-3}), the refractive index hardly differs from unity:

$$n_e - 1 \simeq 10^{-18}.$$

Nevertheless, in matter the neutrino acquires an effective mass that may be significantly different from its rest mass. In 1985, Mikheyev & Smirnov (23) made a revolutionary insight: Depending on the level order for neutrino masses, the effective masses for propagating neutrinos of different flavors could become identical at a certain matter density, inducing a resonance-like behavior that mixes the two states and creates an avoided crossing even if the vacuum mixing angle is very small. Under these conditions, a neutrino that begins as an electron neutrino could emerge as another flavor or combination of flavors.

Up to this time (1985), physicists had been reluctant to embrace the neutrino oscillation solution because the factor-of-three deficit reported by Davis would have required either maximal mixing of three flavors, very unlike quark mixing, or a particular solution in which the oscillation wavelength was 2 AU (24). Both choices seemed improbable. With the discovery of the Mikheyev–Smirnov–Wolfenstein (MSW) matter-enhancement mechanism, a broad range of solutions with small vacuum mixing angles between only two neutrinos suddenly became possible. [Ironically, the solution chosen by nature turned out to have both a large mixing angle (LMA) and MSW enhancement.] The familiar triangle (**Figure 3**) that delineates the sensitivity of a particular solar

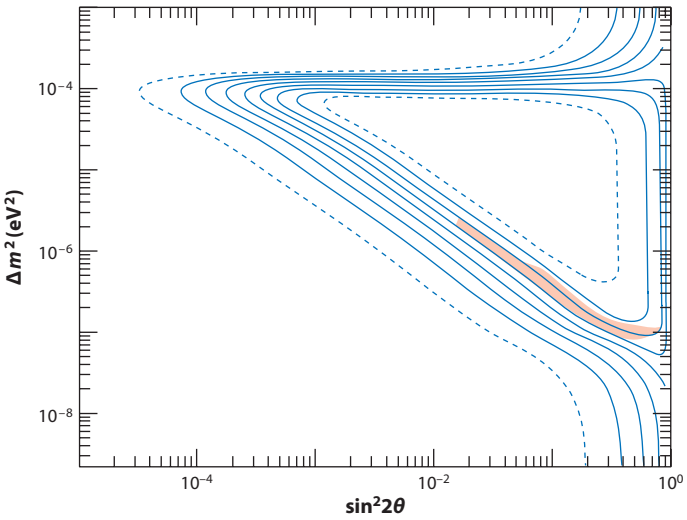

Figure 3

MSW-enhanced survival-probability contours in 10% steps in the $\Delta m^2 - \theta$ plane for the mixing of the ν_1 and ν_2 neutrinos to which the SNO experiment is sensitive (25). The light red shaded area near the bottom is consistent with the Cl-Ar data, the Kamiokande data, and the first data from SAGE (26). Reproduced from Reference 25 with permission from the APS.

neutrino experiment in the presence of MSW enhancement was calculated for the SNO detector in 1992 by Balantekin & Loreti (25).

The MSW effect also leads to a marked difference in the flavor content of the solar neutrino flux between night and day from Earth-regeneration effects for certain regions of the $\Delta m^2 - \theta$ plane, as pointed out by Cribier et al. (27) and by Baltz & Weneser (28). For the modern best-fit solution, the expected day-night asymmetry is only ~3%, however.

Neutrino oscillation is not the only particle physics solution to the solar neutrino problem to have been proposed, but given the steadily improving data [particularly those from SNO and the KamLAND reactor experiment (29)], the other theories have fallen into disfavor. Neutrino decay (30) requires an implausibly large coupling constant and does not give solar and reactor neutrino spectra in agreement with observation. Resonant spin-flavor precession (31) is a phenomenon similar to the MSW effect, except that the effective mass shift and level crossing are provided by the Sun's internal magnetic fields acting on neutrino magnetic moments. Even if this effect were present, it is subdominant in view of the good agreement between terrestrial reactor data and solar data. Possible violations of the weak equivalence principle or of Lorentz invariance by neutrinos seem unlikely for the same reason, and quite impressive limits on such violation, of order 10^{-21}, can be set (32).

4. PHYSICS CAPABILITIES OF THE SUDBURY NEUTRINO OBSERVATORY

SNO's unique physics capabilities arise from the three separate reactions that were used for its detection of ^{8}B solar neutrinos,

$$\nu_e + d \rightarrow p + p + e^- - 1.44\,\text{MeV (CC)},$$

$$\nu_x + d \rightarrow p + n + \nu_x - 2.22\,\text{MeV (NC)}, \quad \text{and}$$

$$\nu_x + e^- \rightarrow \nu_x + e^- \text{ (ES)},$$

where $x = e$, μ, and τ. The CC reaction on deuterium is sensitive only to electron neutrinos, and it provided an energetic electron that produced Cherenkov light in the heavy water. The NC reaction is equally sensitive to all active neutrino types above threshold. The cross section for the ES reaction is smaller than the other reactions and is sensitive to all active neutrino types, with an approximately sixfold larger sensitivity for electron neutrinos at solar energies. Comparing the flux of neutrinos observed through the CC reaction to that observed through the ES or NC reaction could therefore provide evidence for neutrino flavor change, irrespective of the predictions of solar models.

The MSW effect (21, 23) can result in neutrinos above a few megaelectronvolts emerging from the Sun in essentially pure ν_2 states, for instance, for oscillation parameters in the LMA region. To the degree to which this statement is true, SNO's CC/NC ratio, a direct measure of the ν_e survival probability, is also a direct measure of $|U_{e2}|^2$, approximately equal to $\sin^2\theta_{12}$.

The CC reaction produces an electron with an energy nearly equal to the incoming neutrino, less the 1.44-MeV Q-value, and therefore provided spectral information. It has a weak directional sensitivity. The ES reaction produces an electron traveling in nearly the same direction as the incident neutrino but with energies less correlated to those of the incident neutrinos. The NC reaction gives no directional information about the neutrino source, as it produces a free neutron that is quickly thermalized in the heavy water.

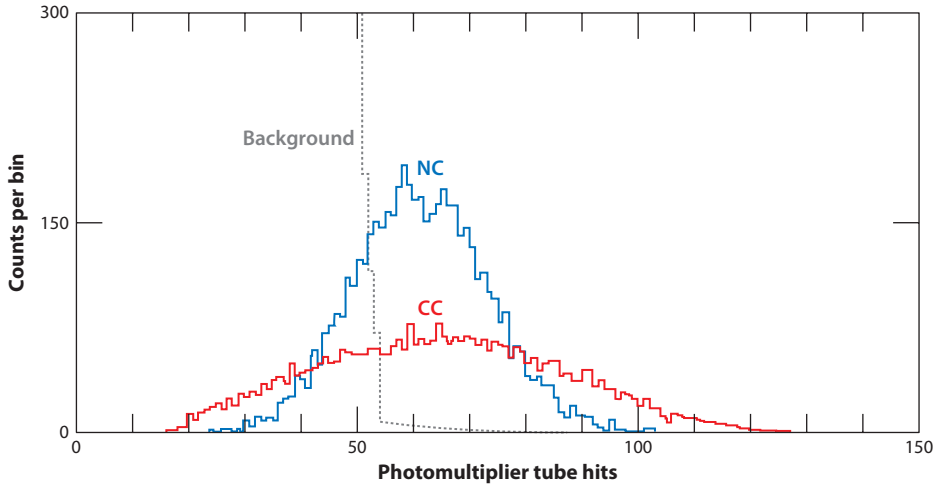

Figure 4

The spectrum predicted in 1987 in the Sudbury Neutrino Observatory proposal (33) for the charged-current (CC; *red line*) and neutral-current (NC; *blue line*) reactions and for the background with a ^{8}B ν_e flux of 2×10^6 cm^{-2} s^{-2} and a total ν flux of 6×10^6 cm^{-2} s^{-1}. It was assumed that 2.5 tonnes of NaCl would be added to the 1000 tonnes of heavy water and that the photocathode coverage would be 75%.

In Phase One of SNO's operation, in which pure heavy water was used, neutron detection occurred through capture on the deuterons in the heavy water with the release of a 6.25-MeV gamma ray. The gamma rays Compton-scattered atomic electrons, and the electrons above the Cherenkov threshold produced Cherenkov light. In Phase Two, 2 tonnes of NaCl were added to the heavy water so that the neutrons from the NC reaction were mainly captured on ^{35}Cl, producing a cascade of gammas with a total energy of ~8.6 MeV. The total capture probability was enhanced, and the pattern of light produced by these gamma cascades was generally more isotropic than the Cherenkov light cone produced by the single electrons from the CC reaction, enabling the two reactions to be statistically distinguished.

The predicted energy spectrum given in the 1987 SNO proposal (33), which included 2.5 tonnes of NaCl added to the 1000 tonnes of heavy water (with 75% photocathode coverage), is shown in **Figure 4**. As discussed in Section 8.8 below, the spectrum observed 15 years later in 2002 was very similar to that originally predicted.

In Phase Three, an array of ^{3}He-filled proportional counters was deployed in pure heavy water in the central acrylic vessel of the SNO detector (34). This so-called neutral-current detection (NCD) array provided a measure of the number of neutrons from the NC reaction that was independent from the light observed by the photomultiplier tubes (PMTs), allowing a separate but simultaneous measurement of the CC and NC reactions.

In SNO, the energy of an event was calibrated in terms of electron kinetic energy and is termed the effective kinetic energy, $T_{\rm eff}$. The threshold for the observation of light from the Cherenkov process was limited by radioactive backgrounds to be above $T_{\rm eff} \sim 4$ MeV, restricting the solar neutrino measurements to neutrinos from ^{8}B decay and the *hep* ($^3\mathrm{He} + p \rightarrow {}^4\mathrm{He} + e^+ + \nu_e$) reaction. The level of radioactive contamination had to be extremely low, particularly in the heavy water, where levels of less than 3.5×10^{-15} g ml^{-1} of Th and 2.7×10^{-14} g ml^{-1} of U were required. These levels ensured that the neutron production occurring through photodisintegration of deuterium was small compared to that from solar neutrino NC interactions.

The ^{8}B neutrinos were the principal focus: The initial objective was to determine the ratio of the flux of electron neutrinos to the flux of all active neutrino types. The data analysis for these measurements is described in detail in Section 8 below. The *hep* reaction was predicted to have a much lower flux than the ^{8}B neutrinos, but because *hep* neutrinos have an end point that extends several megaelectronvolts beyond the end point for ^{8}B neutrinos, it is possible to set a limit on their flux with a careful analysis (described in Section 9 below).

SNO's large target mass, coupled with its very low radioactivity, meant that it was possible to set stringent limits on a number of hypothesized or rare processes, such as neutrinos from a supernova, or limits on the rate for "invisible" nucleon decay. These studies are described in Section 9.

5. THE DEVELOPMENT OF THE SUDBURY NEUTRINO OBSERVATORY

The first collaboration meeting for SNO was held in 1984. It built on efforts begun by Ewan and others (35) to establish an underground laboratory in Canada as well as on ideas from Chen (4, 36) about using heavy water to solve the solar neutrino problem. Previously, T.L. Jenkins of Case Western University (35) had placed a limit on the solar electron neutrino flux using a small heavy water detector. Chen's paper described the possibility of a detector large enough to provide a sensitive measurement and the possibility of using the NC reaction on deuterium to observe all neutrino types. Details of the early days of the collaboration can be found in an article by Ewan & Davidson (37), and descriptions of the early designs are contained in References 38 and 39.

The original collaboration included Atomic Energy of Canada Ltd. (Chalk River Laboratories), Carleton University, Laurentian University, the National Research Council of Canada, Oxford University, Princeton University, Queen's University, University of California at Irvine, and the University of Guelph. A design for a 1000-tonne heavy water detector was established with research and development funding from government agencies and universities. Following the untimely death of Chen in 1987, Art McDonald took over as U.S. spokesman, and he was joined in 1987 by Eugene Beier of the University of Pennsylvania. Los Alamos National Laboratory, Lawrence Berkeley National Laboratory, the University of British Columbia, and Brookhaven National Laboratory joined the collaboration in 1988–1989. In 1989, McDonald moved to Queen's University and became director both of the SNO Institute, where he assumed responsibility for the international project, and of the SNO collaboration. Hamish Robertson became cospokesman in the United States, and David Sinclair and McDonald served as cospokesmen in Canada. U.K. cospokesmen over the years have included Sinclair, Neil Tanner, David Wark, Nick Jelley, and Steve Biller.

Capital funding from Canada, the United States, and the United Kingdom was obtained in 1990; thereafter construction began, with the SNO Institute providing oversight and with Monenco, Ltd. providing project management and engineering services. Specific responsibilities were assigned to groups of scientists or institutions, with group leaders responsible for parts of the detector such as laboratory systems, PMTs, PMT support structure (PSUP), electronics, water systems, etc. The international responsibilities were spelled out in a memorandum of understanding, which assigned capital costs and later operating costs for this international experiment.

This project would not have been possible without the strong support and cooperation of Atomic Energy of Canada Ltd. (AECL), which enabled the loan of 1100 tonnes of heavy water from its reserves with the assistance of Ontario Hydro (now Ontario Power Generation), and INCO Limited (now Vale-INCO), which provided the underground location, only charging incremental operations costs. After they were approached by SNO scientists, senior officials of both these companies became intrigued by the potential for the project, and they were instrumental

in convincing their management to provide this assistance. A basic science project of this scale was very unusual in Canada, and its success depended in large part on strong support from local government officials, universities, and provincial and federal agencies.

The project was international from the outset, with substantial support from U.S. and U.K. funding agencies. Peer review was very important throughout, and the project passed repeated reviews, culminating in a joint international review of the full project design and capital estimates chaired by Ed Temple of the U.S. Department of Energy in 1989. Subsequent to this meeting, a SNO agency review committee consisting of representatives from the Canadian, U.S., and U.K. funding agencies, senior scientists, and technical experts was established. This committee met twice per year to review the project and provide advice to the project management and to the agencies. This process worked well and kept all partners informed of the status, successes, and challenges of the project. Many aspects of the work done to build support for this project beyond peer review assessment are described in Reference 37.

6. THE DESIGN AND CONSTRUCTION OF THE SUDBURY NEUTRINO OBSERVATORY

Figure 5 shows a schematic drawing of the SNO detector. The detector consisted of 1000 tonnes of ultrapure heavy water (99.917% ^{2}H by mass) contained within a 12-m-diameter, 5.6-cm-thick transparent acrylic vessel. The heavy water was viewed with the aid of 9438 sensitive PMTs on an 18-m-diameter support structure. Highly enriched heavy water was required because the neutron-capture cross section on ^{1}H is 640 times that on ^{2}H, establishing a standard of 99.85% enrichment. The entire cavity outside the acrylic vessel was filled with ultrapure light water.

This large cavity was carefully designed to withstand the enormous stresses in the rock at this depth and extensively instrumented to observe the geophysical response following excavation. The inner surface of the cavity was stabilized by the application of wire screening, fastened far into the stable rock with cables, covered by a layer of porous "geotextile," and oversprayed with concrete and a 0.8-cm-thick polyurethane plastic layer designed to reduce the radon permeation from the rock by a factor of ∼100,000. The cavity was initially designed as a 20-m-diameter cylinder, but more advanced modeling indicated that a barrel-shaped design was preferable, enabling a spherical detector geometry that was particularly suited to the incorporation of light collectors on the PMTs. However, the SNO logo (see **Figure 5**), a historical oddity, uses the cylindrical shape in its O.

6.1. Photomultiplier Tubes

The detector's energy threshold was strongly affected by the radioactivity in the PMT components, which were carefully assayed (40). Because glass was the dominant contributor, Schott Glaswerke produced for SNO a new borosilicate glass (Schott 8246), with Th and U impurity levels below 40 ppb, using a furnace with a special low-radioactivity liner. After extensive testing (41) of various PMTs, the Hamamatsu R1408 PMT was selected for use in SNO. This relatively small (20-cm) tube was a manageable size for the thick-walled, mouth-blown Schott 8246 glass envelopes designed to resist stress corrosion in ultrapure water under pressure. Tests and calculations also showed that the collapse of a tube did not pose a risk to neighboring tubes or to the acrylic vessel.

The detector contained 9438 inward-facing PMTs, which provided a photocathode coverage of 31%. To improve the light-collection efficiency, a 27-cm-entrance-diameter light concentrator was mounted on each PMT, increasing the effective photocathode coverage to ∼54% (42). Another 91 PMTs without concentrators were mounted facing outward to detect light from muons and other sources in the region exterior to the PSUP. The light concentrators increased the effective

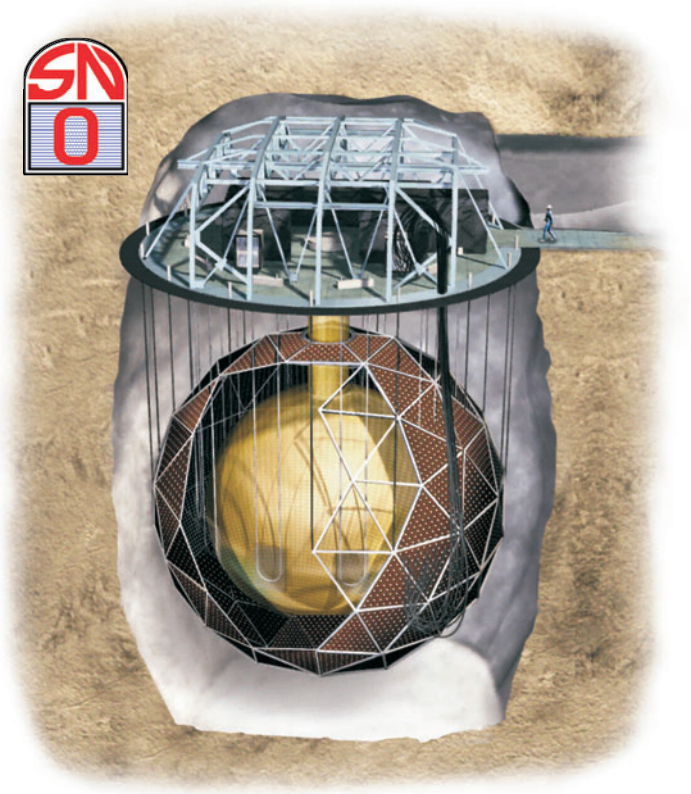

Figure 5

A schematic drawing of the SNO detector, which is located in a 34-m-high by 22-m-diameter barrel-shaped cavity 2039 m below the surface in an active nickel mine owned by Vale-INCO near Sudbury, Ontario, Canada.

area of the photocathode to maximize the number of photons detected and limited the angular acceptance of the photomultipliers so that the detector was viewed by each PMT out to a radius of only 7 m. This setup both reduced background and increased the neutrino signal from the D_2O. The concentrators were made of 18 curved pieces of thin dielectric-coated aluminum sheet, whose outer layer of mixed titanium and praseodymium oxides gave good protection in water.

The PSUP was a geodesic sphere that functioned as the main support system and held the panel arrays that housed the PMTs and light concentrators. The PMTs were secured in hexagonal ABS (acrylonitrile butadiene styrene) black plastic housings that also supported the light concentrators (42) for each inward-facing PMT. The PSUP also provided a water and optical barrier between the core of the experiment (the D_2O-target and light-collection surfaces) and the outer regions of the experiment. This barrier shielded the PMTs from light generated in the water surrounding the PSUP and also functioned as a highly impermeable barrier to any contamination in that water.

All the materials used in the construction of the PSUP were carefully selected to be of low radioactivity. Originally the design of the PSUP included aluminum, but careful measurements (43) taken at the Lawrence Berkeley Laboratory cyclotron determined that gammas produced by nuclear reactions induced by the inherent alpha radioactivity in aluminum would be unacceptable, requiring a complete change from the original aluminum design to a stainless steel structure.

6.2. Electronics and Data Acquisition

The electronics chain was required to provide subnanosecond-time and wide dynamic-range charge measurement for the PMT pulses. Although the solar neutrino event rate was very low, the electronics chain had to process background rates in excess of 1 kHz and burst rates from potential supernovae in excess of 1 MHz without significant dead time. The first-level hardware trigger for detection of solar neutrinos was a simple count of the number of PMTs that had fired within a window of ∼100 ns, which allowed for light transit across the 17-m-diameter PMT array and which was done via a chain of analog summations. A built-in pulser provided a pulsed global trigger, which sampled backgrounds as a "zero-bias" trigger for the detector at a rate of 5 Hz.

The readout of the electronics was both controlled and monitored via a user-interface program, the SNO hardware acquisition and readout control (SHARC). SHARC also controlled SNO's calibration sources through a manipulator computer. For further details about SHARC's operation, see Reference 44.

For the third phase of running with the NCD array, signals from the independent data-acquisition hardware (34) for the NCD array and the PMT array were integrated in a global trigger system that combined both data streams with timing information for the events. The NCD electronics were controlled by the object-oriented real-time control and acquisition (ORCA) system (45). SHARC could remotely supervise ORCA, keeping run numbers and data acquisition synchronized between the NCD and PMT systems.

6.3. Acrylic Vessel

The acrylic vessel, 12 m in diameter and 5.6 cm thick, contained the 1000 tonnes of heavy water. Because the vessel had to have uncompromising integrity as well as excellent transparency and very low radioactivity, ultraviolet-transmitting (UVT) acrylic was chosen as the material. Acrylic is used in windows for large-scale aquaria and in diving bells made for human occupancy. To allow the insertion of piping and calibration devices and the installation of the ^{3}He neutron–detector strings, the sphere was provided with a 1.5-m-diameter by 6.8-m-high chimney. The vessel was suspended from 10 Vectran ropes that passed through U-shaped grooves cut into double-thickness panels at the equator.

When this engineering project began in 1990, no one had constructed an acrylic sphere of comparable size, especially not 2 km underground in ultraclean conditions. Bonding the acrylic panels to form a sphere involved careful positioning at ∼3 mm separation, pouring bonding material between dams, and curing and annealing the polymerized material. In a few areas there were flaws, such as exothermic bubbles, that required a section of the bond to be cut out. These repairs required the development of specific techniques to bond unusually shaped pieces. These techniques were developed through an extensive effort over several years by members of the SNO collaboration and personnel from Reynolds Polymer Corporation, the principal contractor.

Radioactivity in the fabrication of the panels for the vessel was carefully controlled. Concentrations of ^{232}Th and ^{238}U in acrylic samples taken from each panel were measured to be less than the specified 1.1 pg g^{-1} by neutron-activation analysis, mass spectrometry, and alpha spectroscopy. Optical absorption measurements were also performed for each panel.

6.4. Water Systems

A particular challenge was that the heavy water had to contain no more than 3.5×10^{-15} g ml^{-1} of Th and 2.7×10^{-14} g ml^{-1} of U. Several techniques for measuring such low levels were developed (see Section 6.5). These low levels required that great care be taken in the selection of materials for

the water systems, in particular for the O-rings, circular gaskets used in sealing the pipes. Initially urethane was chosen, but the radon permeation was far too high. This serious problem was solved only when the O-ring composition was changed to butyl rubber.

There were two water systems at SNO: one for the ultrapure light water (H_2O) and one for the heavy water (D_2O). These systems were located underground, near the detector. For the H_2O, potable water for the mine was pretreated with filters, then purified through use of charcoal filters and the addition of EDTA to complex various ion species before passing through a large reverse-osmosis unit. The water then entered a UV unit, where any remaining organic compounds were dissociated, before flowing through ion-exchange units.

A degassser reduced the levels of oxygen and radon in the water, so as not to support biological activity as well as to minimize radioactivity. During the filling of the detector, it was discovered that degassed water compromised the breakdown voltage of the PMT connectors. This was caused by diffusion of air out of the PMT high-voltage connectors into the degassed water. To avoid this serious problem, the water was regassed with pure N_2 using a gas permeable–membrane unit. Finally, a chiller cooled the water to 10° C before it went into the cavity. The H_2O was continuously circulated to remove ions, organic materials, and suspended solids.

The source of the D_2O was the Ontario Power Generation's Bruce Heavy Water Plant beside Lake Huron. The 1100 tonnes of heavy water from AECL were exchanged with D_2O from Ontario Power Generation that had been extracted directly from the lake and had very low tritium content. The heavy water was first passed through ion-exchange columns to reduce its ionic content, in particular its K content, before it went into the acrylic vessel. After the SNO detector was filled, the D_2O was recirculated to maintain its purity, and it was regularly assayed to measure its radioactivity.

To purify the NaCl before it was added to the heavy water for Phase Two, a small purification plant that included both MnOx and HTiO filters was built. To take the NaCl out of the water after the second phase of SNO running, the heavy water was passed through reverse-osmosis units to reduce the concentration of NaCl to a few parts per million.

6.5. Radioactivity Control and Measurement

Minimizing background events required a high intrinsic radioactive purity of materials. This was addressed at the time of material selection by measuring the activity of samples from all detector materials. Low-background gamma-ray counting and neutron-activation analysis were used extensively for such measurements. Extensive measurements of leach rates and radon emanation were carried out for all critical materials. To prevent radon (at a concentration of 3 pCi liter^{-1} in the laboratory air) from getting into the D_2O and H_2O, a cover gas system provided nitrogen gas that functioned as a physical barrier between the water and the radon-rich laboratory air.

Contamination with radon, Th, and U was of particular concern because gamma rays with energy greater than 2.2 MeV can photodisintegrate deuterium, and the neutron thus produced would be indistinguishable from a neutron produced through the NC interaction of solar neutrinos. The expected NC neutron-production rate based on solar models was ~14 per day. To make neutrons from photodisintegration tractable, the radioactivity requirements on the levels of Th and U chain nuclei in the heavy water were set so that each did not give rise to more than one neutron per day. These settings gave limits of 3.5×10^{-15} g ml^{-1} of ^{232}Th and 2.7×10^{-14} g ^{238} ml^{-1} of U. The requirement for the light water surrounding the heavy water was less stringent, with upper limits of 3.5×10^{-14} g ml^{-1} of ^{232}Th and of 4.1×10^{-13} g ml^{-1} of ^{238}U.

The nuclei in the Th and U chains that emit gamma rays with energies greater than 2.2 MeV are ^{208}Tl and ^{214}Bi, respectively. The isotope ^{208}Tl is supported by the radium isotope ^{224}Ra, whereas ^{214}Bi is supported by ^{226}Ra and ^{222}Rn. Three ex situ techniques were developed to assay

the precursor radioisotopes of ^{208}Tl and ^{214}Bi in the D_2O and H_2O. The decays of the parent Rn and Ra isotopes were counted in systems external to the SNO detector (46–48).

During neutrino data taking, an in situ method based on the Cherenkov light produced by the radioactivity in the water was developed to assay ^{208}Tl and ^{214}Bi. The Cherenkov light in the analysis window $\sim 4.0 \leq T_{\rm eff} \leq 4.5$ MeV effective electron kinetic energy is dominated by that from the beta-gamma decay of ^{208}Tl and the beta decay of ^{214}Bi. The anisotropies of the Cherenkov light from these decays are different: The Cherenkov light from ^{208}Tl is more isotropic than that from ^{214}Bi. The different hit patterns of ^{214}Bi and ^{208}Tl events allowed the distribution of event isotropy (characterized in Phase One by the mean angle between PMT pairs, θ_{ij}) to be used to statistically separate the ^{208}Tl and ^{214}Bi decays. The parameter θ_{ij} was calculated by taking the average angle relative to the reconstructed event vertex for all hit PMT pairs. In Phases Two and Three, the event isotropy was characterized by a function of θ_{ij}, β_{14} (see Section 8.7 below).

6.6. Calibration Sources

A general-purpose manipulator was developed to provide deployment of calibration sources at accurately known off-axis positions in two orthogonal planes in the D_2O. A ^{16}N source (49) provided a 6.13-MeV gamma ray following its beta decay, allowing these gammas to be used as a primary energy calibration by triggering on the beta. Both electrons from a ^{8}Li source (50) and 19.8-MeV gammas, produced with a small accelerator via the $^{3}H(p, \gamma)\,^{4}He$ reaction, were used to verify the energy scale for higher-energy electrons.

To determine the principal optical properties of the detector, a so-called laser ball source (51) was used to diffuse the laser light from an external pulsed nitrogen laser or dye laser at wavelengths ranging from 337 to 620 nm. Electronic pulsers were regularly used to define the characteristics of the signal-processing electronic circuits and the data-acquisition systems.

To calibrate the neutron response, sources of ^{252}Cf encapsulated in acrylic were employed, as were ^{241}AmBe sources. For the third phase, a distributed source of ^{24}Na was used to measure the neutron response and efficiency of the NCD array. The 2.754-MeV gammas from neutron-activated NaCl dissolved in the heavy water photodisintegrated deuterium and created a nearly uniform and homogeneous source of neutrons.

Measured amounts (spikes) of ^{222}Rn were added to both the heavy water and the light water. The resulting data, together with those from sources of ^{238}U and ^{232}Th, were used to simulate the signals coming from trace radioactive contamination. For all the point sources, multiple layers of acrylic encapsulation were used to ensure that no trace amount of radioactivity could be introduced during the source deployment.

7. GENERAL DESCRIPTION OF ANALYSIS

Data processing began with the calibration of the raw data and the conversion of analog-to-digital converter values into PMT charges and times. The calibrated charges and times were used to reconstruct each event's position and direction and to estimate event energy. At later stages of the data processing, cuts were applied to the data set to remove as many background events as possible without rejecting a substantial number of neutrino signal events. A similar procedure was used for the data from the NCD array (34), and the calibrated charges from the NCD array were used to estimate the event energy.

7.1. Analysis and Simulation Code

The off-line software is required to perform two major functions: (*a*) analysis of SNO data and (*b*) detailed and complete simulation by Monte Carlo techniques of all significant signals and

backgrounds that employs as accurate a model of the detector and its response as possible. Both of these functions were combined in the SNO Monte Carlo and analysis code (SNOMAN).

SNOMAN consists of a set of largely autonomous processors written primarily in FORTRAN. These processors communicate through a central data structure managed by the CERNLIB package ZEBRA (52). ZEBRA is also the basis for the management of banks of data, known as titles. Title-management routines in SNOMAN ensure that as successive events are analyzed the constants describing the detector response are appropriate for that time and detector configuration. A more detailed description is given in Reference 44.

In addition to SNOMAN, there is another major off-line analysis tool: the SNO database (SNODB), which is based on the CERNLIB package HEPDB. SNODB is a distributed master-slave database that runs collaboration-wide via PERL installation and management scripts. Other analysis tools include (*a*) QSNO, which provides interfaces to ROOT analysis platforms; (*b*) QPhysics, which is a platform for MSW mixing analysis; and (*c*) various signal-extraction packages that extract the three neutrino-interaction rates using extended maximum-likelihood fits to the data.

7.2. Distributions of Events from the Three Neutrino Reactions

The light detected by the PMTs was used in the first two phases of the experiment to determine the rates of events observed from the three reactions (CC, NC, and ES). In the third phase, this information was supplemented by the events detected by the NCD array, which provided the primary information for the NC reaction. Each observed event was reconstructed to obtain information about the energy, location, time, and direction (where relevant) of the event. Information from calibration sources was also used to estimate systematic uncertainties in the reconstructed quantities. The full set of available information was used to provide a statistical separation of the events from the three reactions by performing a generalized maximum-likelihood fit to the array of events.

As an example, **Figure 6** shows simulated probability density functions (pdfs) for each of the signals for Phase One, which used pure D_2O. The energy distributions for each of the three signals are shown in **Figure 6*a***. The strong correlation between the electron energy and the incident neutrino energy for the CC interaction produces a spectrum that resembles the initial ^{8}B neutrino spectrum, whereas the recoil spectrum for the ES reaction is much softer. Within the smearing of the Compton-scattering process and the resolution of the detector, the NC reaction produces what is essentially a line spectrum because the gamma produced by the neutron capture on deuterium always has an energy of 6.25 MeV.

The distributions of reconstructed event positions $(R/R_{AV})^3$, normalized to the radius of the acrylic vessel, R_{AV}, are shown in **Figure 6*b***. The CC reaction, which occurs only on deuterons, produces events distributed uniformly within the heavy water, whereas the ES reaction, which can occur on any electron, produces events distributed uniformly well beyond the heavy water volume. The small leakage of events just outside the heavy water volume (just outside $(R/R_{AV})^3 = 1$) for the CC reaction is due to the resolution tail of the reconstruction algorithm.

The NC signal does not have a uniform distribution inside the heavy water, but instead it decreases monotonically from the central region to the edge of the acrylic vessel. The reason for this nonuniform distribution is the long (~120-cm) diffusion length for thermal neutrons in D_2O, which results in a significant fraction of the neutrons being captured on hydrogen in the acrylic or in the surrounding light water. For the second phase of the project, the distribution of NC events was much flatter until close to R_{AV} because the capture on ^{35}Cl dominated the events compared to leakage into the acrylic and H_2O.

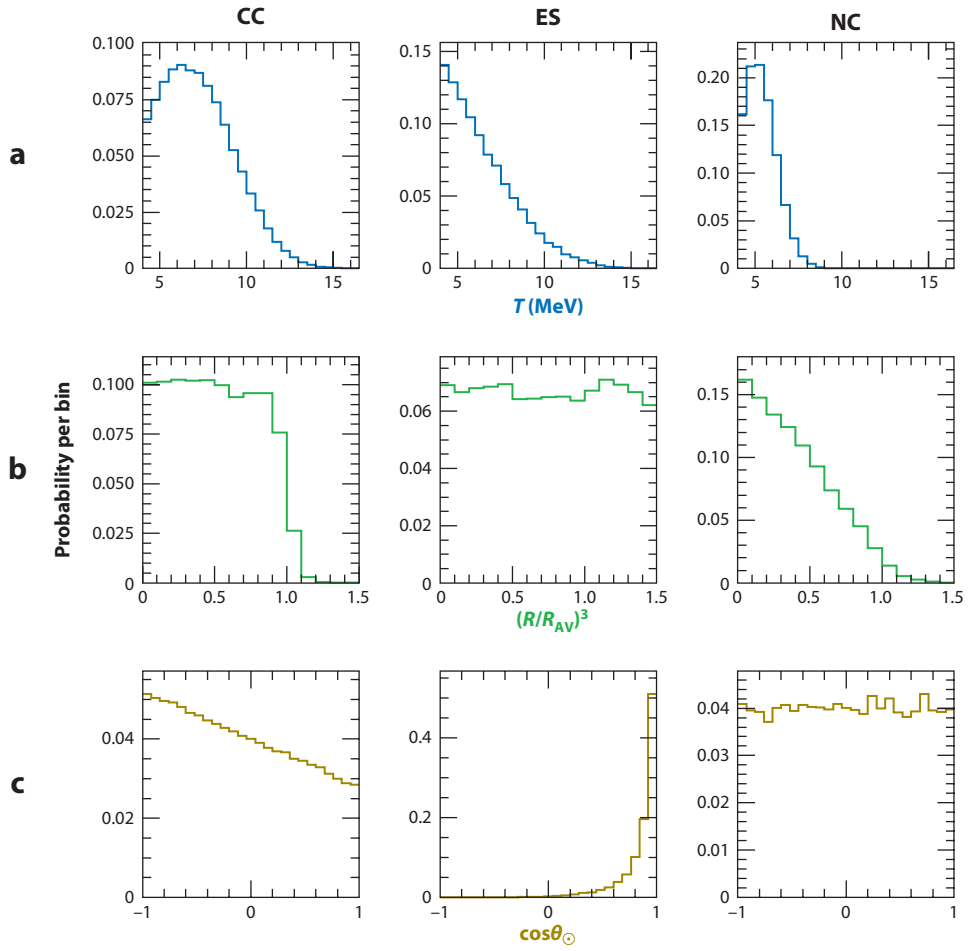

Figure 6

The (*a*) energy, (*b*) radial, and (*c*) directional distributions used to build probability density distributions to fit the SNO signal data. Abbreviations: *T*, the kinetic energy of the electron from the charged-current (CC) or elastic scattering (ES) reactions or from the gamma interaction following neutron capture; NC, neutral-current reactions; R/R_{AV}, the reconstructed event radius normalized to the 600-cm radius of the acrylic vessel.

Figure 6*c* shows the reconstructed direction distribution of the events. The peaking of the ES reaction clearly points away from the Sun, and the $1 - \frac{1}{3}\cos\theta_{\text{Sun}}$ distribution of the CC reaction is also apparent. The NC reaction shows no correlation with the solar direction: The gamma ray from the captured neutron carries no directional information about the incident neutrino.

The NC-labeled distributions in **Figure 6** represent equally well the detector response to any neutrons, not just those produced by NC interactions, as long as the neutrons are distributed uniformly in the detector. An example is neutrons produced through photodisintegration by gamma rays emitted by radioactivity in the D_2O. Such neutrons are an irreducible background in the data analysis and were kept small compared to the NC events through careful selection and purification of detector materials. Techniques were developed for the accurate determination of this background of neutron events from photodisintegration of deuterium (see Section 6.5).

7.3. Removal of Instrumental Background Events

In addition to neutrino interactions, cosmic rays, and radioactive decays, the SNO detector also collected and recorded many instrumental background events produced by the detector itself. Because of these events' much higher frequency, a high rejection fraction was needed to ensure they did not contaminate the final data sample. The removal of these instrumental background events by various cuts defined to separate the instrumental events on the basis of a variety of characteristics is described in Reference 53.

Because it was not feasible to model every possible non-Cherenkov background source, it was necessary to develop a method that could determine the background level irrespective of its source. The method adopted for this analysis combined cuts in what is sometimes referred to as a bifurcated analysis. For the final Phase One data set, this technique revealed that the overall contamination had a 95%–confidence level upper limit of $\leq$3 events. For further details, see Reference 53.

In the third phase, instrumental backgrounds in the NCD array such as bursts, oscillatory events caused by electromagnetic transients, "fork" events caused by microdischarge in insulators (mainly near the tops of the delay lines), and blank digitizer traces were removed from the data with cuts that permitted an evaluation of the signal loss and residual background. For further details, see Reference 34.

8. SOLAR NEUTRINOS

8.1. Phase One: Pure Heavy Water

The first operation of the detector utilized pure heavy water as the central detection medium. In this phase, neutron detection occurred through capture on the deuterons in the heavy water with the release of a 6.25-MeV gamma ray. The gamma ray Compton-scattered atomic electrons, and the electrons above the Cherenkov threshold produced Cherenkov light.

Operation began with the empty detector and continued as the levels of heavy water and light water were raised together to minimize the stress on the acrylic vessel over a period of more than nine months. The rate was defined primarily by the shipment schedule of the heavy water to the detector site. This enabled electronic systems to be commissioned and allowed some problems to be corrected, such as the high-voltage-connector problem discussed above.

8.1.2. Data. Full operation with pure heavy water began on November 2, 1999 and ended on May 31, 2001, for a total of 306.4 live days of neutrino data taking. The many days of calibration corresponded to ~10% of the running time. The energy scale and response were determined primarily with the ^{16}N source, together with the other calibration sources described in Section 6.6. The neutron-capture efficiency was measured by deploying a ^{252}Cf source at various positions throughout the heavy water volume. These point-source calibrations were employed, together with Monte Carlo simulation and an analytic diffusion model, to extract the neutron-detection efficiency and its uncertainty. For a threshold of $T_{\text{eff}} = 5$ MeV and a fiducial volume defined by $R \leq 550$ cm, the measured neutron-capture efficiency value was 0.1438 ± 0.0053.

8.1.3. Analysis procedure. To prevent the introduction of statistical bias while cuts were optimized, the data set was divided into two separate sets: an "open" data set, to which all analysis procedures and methods were applied, and a "blind" data set, upon which no analysis within the signal region (between 40 and 200 hit phototubes) was performed until the full analysis program

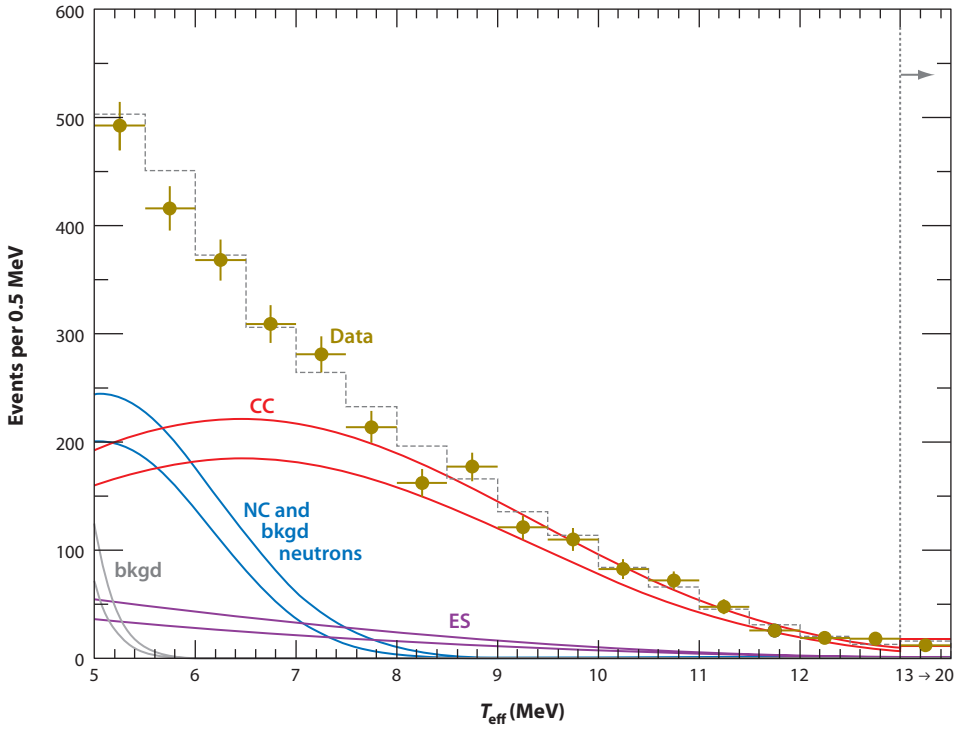

Figure 7

Kinetic energy spectrum for $R_{fit} \leq 550$ cm and $T_{eff} \geq 5$ MeV (*brown data points*). Also shown are the Monte Carlo predictions for charged-current (CC; *red lines*), elastic scattering (ES; *purple lines*), and neutral current (NC) and background (bkgd) neutron events (*blue lines*) scaled to the fit results and the calculated spectrum of beta-gamma background events (*gray lines*). The dashed line represents the summed components, and the bands show the $\pm 1\sigma$ statistical uncertainties from the signal-extraction fit.

had been finalized. The total size of the blind data set corresponded to roughly 30% of the total live time.

The data observed with the PMTs exhibited events from all three detection reactions with the characteristics shown in **Figure 6**. The first detailed analysis (54) aimed at detecting events above an effective kinetic energy of 6.75 MeV, eliminating any significant contributions from the NC reaction or from the low-energy region dominated by radioactive background (see **Figure 7**). The CC and ES reactions could be resolved through use of the strong directional dependence of the ES reaction. A second analysis (55) with an effective kinetic energy threshold of 5 MeV, as well as a fiducial volume inside 550 cm, provided the opportunity to include the NC reaction in the analysis (**Figure 7**).

8.1.4. Results from phase one. The results from the first detailed analysis (54) of events above an effective kinetic energy of 6.75 MeV from the CC and ES reactions provided the following fluxes (assuming an unperturbed shape for the ^{8}B spectrum):

$$\phi_{CC}^{SNO}(\nu_e) = 1.75 \pm 0.07\,(\text{stat.})^{+0.12}_{-0.11}\,(\text{syst.}) \pm 0.05\,(\text{theor.}) \times 10^6\,\text{cm}^{-2}\,\text{s}^{-1} \quad \text{and}$$

$$\phi_{ES}^{SNO}(\nu_x) = 2.39 \pm 0.34\,(\text{stat.})^{+0.16}_{-0.14}\,(\text{syst.}) \times 10^6\,\text{cm}^{-2}\,\text{s}^{-1}.$$

SNO's ES rate measurement was consistent with the precision measurement of the ^{8}B flux taken by the Super-Kamiokande collaboration, which made use of the same ES reaction (56):

$$\phi_{\rm ES}^{\rm SK}(\nu_x) = 2.32 \pm 0.03\,({\rm stat.})^{+0.08}_{-0.07}\,({\rm syst.}) \times 10^6\ {\rm cm}^{-2}\ {\rm s}^{-1}.$$

The difference between the flux $\phi_{\rm ES}^{\rm SK}(\nu_x)$ measured by Super-Kamiokande via the ES reaction and the $\phi_{\rm CC}(\nu_e)$ flux measured by SNO via the CC reaction is $(0.57 \pm 0.17) \times 10^6$ cm^{-2} s^{-1}, or 3.3σ from zero, assuming that the systematic errors are normally distributed. This difference was strong evidence for the presence of nonelectron flavors in the flux and therefore for neutrino flavor change. The total flux of active ^{8}B neutrinos was determined via $\phi_{\rm CC}^{\rm SNO}$ and $\phi_{\rm ES}^{\rm SK}$ to be

$$\phi(\nu_x) = 5.44 \pm 0.99 \times 10^6\ {\rm cm}^{-2}\ {\rm s}^{-1},$$

in excellent agreement with predictions of standard solar models (2, 3, 57). The reference (2) ^{8}B neutrino flux was 5.05×10^6 cm^{-2} s^{-1}.

In the second analysis (55), the effective kinetic energy threshold was 5 MeV, sufficient to resolve the contributions from CC, ES, and NC events above threshold. Background event pdfs were included in the analysis, with fixed amplitudes determined by the background calibration. The extended maximum-likelihood method used in the signal decomposition yielded $1967^{+61.9}_{-60.9}$ CC events, $263.6^{+26.4}_{-25.6}$ ES events, and $576.5^{+49.5}_{-48.9}$ NC events, where only statistical uncertainties are given. Systematic uncertainties on fluxes were derived by repeating the signal decomposition with perturbed pdfs, constrained by calibration data. **Figure 7** shows the energy spectra obtained.

The total neutron background was 78 ± 12 events, of which 71 were from photodisintegration. The total Cherenkov background (the background to CC and ES events) was 45^{+18}_{-12} events. The fraction of neutron events (NC + background) that were due to photodisintegration was therefore 11% (with an uncertainty of less than 2%), evidence that the radioactive cleanliness requirements for SNO had been met.

The results of this analysis gave the following fluxes in units of $\times 10^6$ cm^{-2} s^{-1}:

$$\phi_{\rm CC} = 1.76^{+0.06}_{-0.05}\,({\rm stat.})^{+0.09}_{-0.09}\,({\rm syst.}),$$

$$\phi_{\rm ES} = 2.39^{+0.24}_{-0.23}\,({\rm stat.})^{+0.12}_{-0.12}\,({\rm syst.}), \quad \text{and}$$

$$\phi_{\rm NC} = 5.09^{+0.44}_{-0.43}\,({\rm stat.})^{+0.46}_{-0.43}\,({\rm syst.}).$$

A simple change of variables resolves the data directly into electron ($\nu_{\rm e}$) and nonelectron ($\nu_{\mu\tau}$) components,

$$\phi_{\nu_{\rm e}} = 1.76^{+0.05}_{-0.05}\,({\rm stat.})^{+0.09}_{-0.09}\,({\rm syst.}) \quad \text{and}$$

$$\phi_{\nu_{\mu\tau}} = 3.41^{+0.45}_{-0.45}\,({\rm stat.})^{+0.48}_{-0.45}\,({\rm syst.}),$$

assuming the standard ^{8}B shape. Combining the statistical and systematic uncertainties in quadrature, $\phi_{\nu_{\mu\tau}}$ is $3.41^{+0.66}_{-0.64}$, which is 5.3σ above zero. This result provides additional stronger evidence for flavor transformation consistent with neutrino oscillations. These results are plotted in **Figure 8**.

A further analysis (58) provided information on the day-night asymmetry. For CC events, assuming an undistorted ^{8}B spectrum, the night minus day rate was found to be $14.0 \pm 6.3^{+1.5}_{-1.4}$% of the average rate. When the total flux of active neutrinos was additionally constrained to have

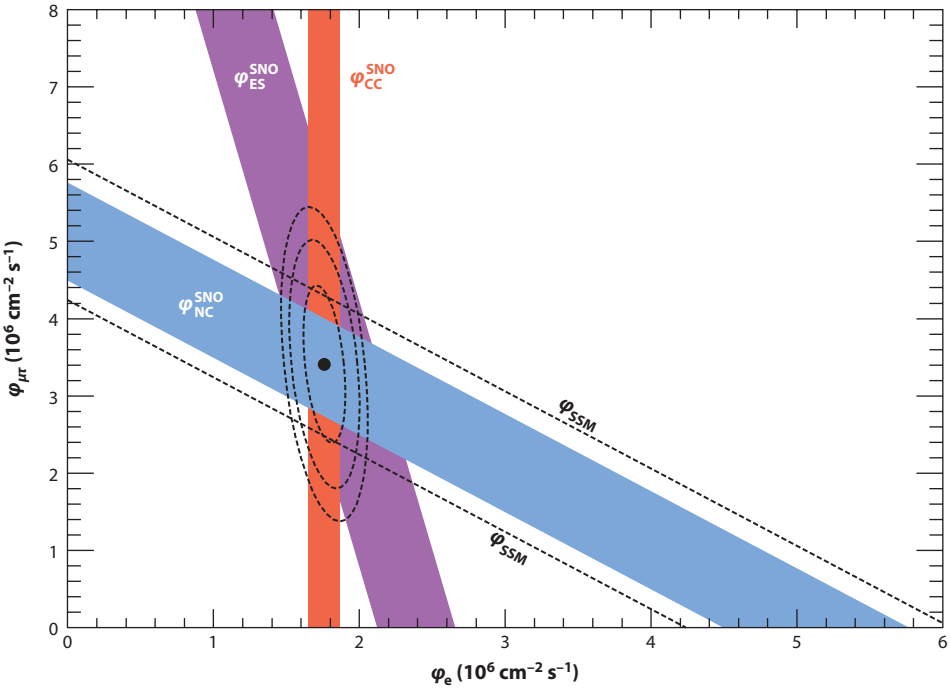

Figure 8

The flux of ^{8}B solar neutrinos of μ or τ flavor versus the flux of electron neutrinos deduced from the three neutrino reactions [charged current (CC; *red*), elastic scattering (ES; *purple*), and neutral current (NC; *blue*)] in SNO. The diagonal bands show the total ^{8}B flux as predicted by the BP2000 Standard Solar Model (SSM) (*dashed lines*) from Reference 2 and that measured with the NC reaction in SNO (*solid blue band*). The intercepts of these bands with the axes represent the $\pm 1\sigma$ errors. The three bands intersect at the fit values for ϕ_{ν_e} and $\phi_{\nu_{\mu\tau}}$, indicating that the combined flux results are consistent with neutrino flavor transformation with no distortion in the ^{8}B neutrino energy spectrum.

no asymmetry, the ν_e asymmetry was found to be $7.0 \pm 4.9^{+1.3}_{-1.2}$%. A global neutrino analysis (59) that included the MSW effect (21, 23) in the Sun favored a LMA solution.

8.2. Phase Two: Salt Added to Heavy Water

The original SNO proposal (33) suggested adding Cl to raise the NC signal above that observed with pure heavy water. The addition of Cl increases the neutron-capture efficiency, and the associated Cherenkov light also increases because more energy is released in the accompanying neutron capture on ^{35}Cl. Furthermore, neutron capture on ^{35}Cl typically produces multiple gamma rays, whereas the CC and ES reactions produce single electrons. The generally greater isotropy of the Cherenkov light from neutron-capture events relative to CC and ES events allowed good statistical separation of the event types and enabled precise measurement of the NC flux, independent of assumptions about the CC and ES energy spectra.

In May 2001, 2 tonnes of purified NaCl were added to the 1 ktonne of heavy water, which increased the neutron-capture efficiency for neutrons generated uniformly in the D_2O by approximately a factor of three from the pure D_2O phase (see **Figure 9*a***). The solution was thoroughly mixed, and a conductivity scan along the vertical axis showed the NaCl concentration to be uniform

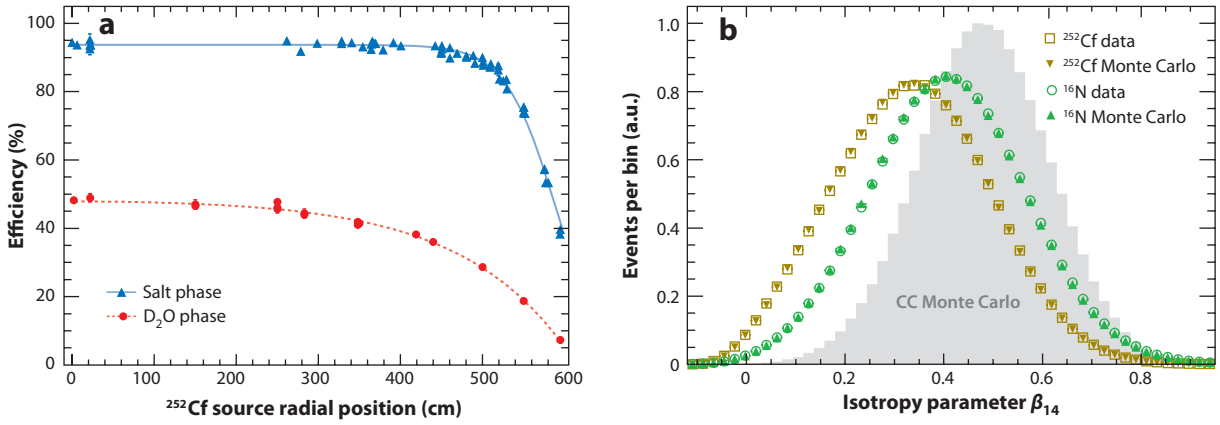

Figure 9

(*a*) Neutron-capture efficiency versus radial position of the ^{252}Cf source for the pure D_2O and salt phase. The solid blue line represents the fit of the salt-phase data to an empirical function (60), and the dotted red line represents the fit of the D_2O-phase data to a neutron-diffusion model. (*b*) β_{14} isotropy distributions for ^{252}Cf data and Monte Carlo (*brown*), ^{16}N data and Monte Carlo (*green*), and simulated charged-current (CC) events (*gray*).

within 0.5%. $MgCl_2$, rather than NaCl, had been considered (44), because of concern about K contamination of NaCl and activation of the ^{23}Na. However, measurements of the radiation near the water-circulation pipes and of K content showed that NaCl was acceptable, even preferable, as it was chemically easier to process.

8.2.1. Data. Phase Two data were collected between July 26, 2001 and August 28, 2003, for a total exposure of 391.4 live days. The measurement and calibration of the detector response were determined using the same sources as in the first phase. In addition, sources of ^{24}Na and ^{222}Rn were used in the D_2O to measure the response to low-energy beta-gamma decays. The ^{24}Na sources were made by deploying a 330-kBq ^{232}Th source in the heavy water: The 2.614-MeV gammas produced neutrons through photodisintegration of deuterons, which occasionally captured on ^{23}Na nuclei. Calibration of the detector's optical and energy response was updated to include time variation in the water-transparency measurements made at various wavelengths throughout the running period. A normalization for photon-detection efficiency based on ^{16}N calibration data and Monte Carlo calculations was used to set the absolute energy scale, which had an uncertainty of 1.1%.

The neutron-detection efficiency was measured with a ^{252}Cf source. The source strength had been determined both with a calibrated array of ^{3}He counters and, after deployment in the heavy water, by time-series analyses of the neutron events (61). In determining the efficiency, the prompt fission gammas emitted in the spontaneous decay of ^{252}Cf had to be taken into account. The efficiency for detecting neutrons that had a reconstructed vertex within $R_{\rm fit} \leq 550$ cm was found to be 0.407 ± 0.010. Details of the energy, optical, and efficiency calibrations are given in Reference 60.

8.2.2. Analysis procedure. Following data-reduction and analysis-selection procedures similar to those carried out in the first phase, the total data set consisted of 4722 events. The effective electron kinetic energy threshold was $T_{\rm eff} \geq 5.5$ MeV, which, together with a fiducial volume cut of radius $R_{\rm fit} \leq 550$ cm, reduced the Cherenkov event backgrounds arising from beta-gamma decays

to 3.5 events. A bifurcated analysis established that the residual contamination of instrumental backgrounds in the neutrino data set was fewer than 3 events.

The separation of NC from CC and ES events was enhanced by utilizing the difference between the isotropy of the Cherenkov light from neutron-capture events and those from CC and ES events. Event isotropy was characterized by parameters β_l, the average value of the Legendre polynomial P_l of the cosine of the angle between PMT hits. The combination $\beta_1 + 4\beta_4 \equiv \beta_{14}$ was selected as the measure of event isotropy to optimize the separation of NC and CC events. Systematic uncertainty on β_{14} distributions generated by Monte Carlo for signal events was evaluated by comparing ^{16}N calibration data to Monte Carlo calculations for events throughout the fiducial volume and running period. The uncertainty on the mean value of β_{14} was 0.87%. Comparisons of β_{14} distributions from ^{16}N events and neutron events from ^{252}Cf to Monte Carlo calculations are shown in **Figure 9*b***.

Initially, a discrepancy of approximately 2.5% between data and Monte Carlo was observed in β_{14}. Good agreement was obtained after a small correction was made to EGS4 (62) to account for approximations used in the description of electron scattering in the Monte Carlo simulation, mainly for the neglect of the Mott terms (60).

The principal backgrounds were from natural radioactivity in the heavy water and in the acrylic vessel. The backgrounds in the heavy water were measured by the in situ and ex situ methods described in Section 6.5 above. For the in situ technique used in Phase Two, the isotropy of the Cherenkov light from decays of ^{208}Tl and ^{214}Bi was characterized by the decays' β_{14} distributions, rather than by their θ_{ij}, distributions. A small amount of ^{24}Na was produced by calibration sources deployed in the heavy water and by radiation activating ^{23}Na in the water-circulation pipes, and the contribution from ^{24}Na decays was taken into account in the in situ analysis. The total number of neutrons from internal sources was $125.1^{+37.3}_{-32.0}$, of which $91.3^{+30.4}_{-31.5}$ came from photodisintegration by Th and U chain activity, corresponding to only 6% of the NC events. A table listing all the background contributions is provided in Reference 60.

During construction of the acrylic vessel, Rn progeny accumulated on the vessel's surfaces. These daughters initiated (α, n) reactions on ^{13}C, ^{17}O, and ^{18}O. Also, a few external gamma rays originating from radioactivity in the construction material of the detector and the rock cavity entered the D_2O target and photodisintegrated deuterons. The radial distribution of these neutrons peaked near the acrylic vesssel, and the enhanced neutron-detection efficiency in the second phase of SNO made it possible to extract this external-source neutron contribution in the neutrino signal window by including an additional radial distribution function in the statistical analysis of the solar neutrino flux.

The data were analyzed to give day and night neutrino fluxes. The systematics on the asymmetry ratio $A = 2(\phi_N - \phi_D)/(\phi_N + \phi_D)$ were evaluated using classes of events that were continually present in the detector. These consisted primarily of secondary neutrons produced in the D_2O by throughgoing muons and Cherenkov events from low-energy beta-gamma decays. A localized region of higher than average background radioactivity was discovered on the upper surface of the acrylic vessel. This hot spot provided an excellent check of position reconstruction for a point source of events. Variations in detector response with the direction of an event were taken into account, as such variations could produce a day-night systematic for neutrino signals, which have different directional distributions for night and day.

A blind analysis procedure was used in the analysis of the first 254.2 live days of data (63): The data set used during the development of the analysis procedures and the definition of parameters (*a*) excluded an unknown fraction (<30%) of the final data set, (*b*) included an unknown admixture of neutrons from muon-produced spallation background events in the analyzed data set, and (*c*) included an unknown NC cross-section scaling factor in signal simulations. After fixing all

analysis procedures and parameters, the blindness constraints were removed. The analysis was then performed on the open data set, statistically separating events into CC, NC, ES, and external-source neutrons using an extended maximum-likelihood analysis based on the distributions of isotropy (β_{14}), the cosine of the event direction relative to the vector from the Sun, and the radius within the detector.

This analysis differs from that of the pure D_2O data because the spectral distributions of the ES and CC events were not constrained to the ^{8}B shape, but rather were extracted from the data. To obtain the electron energy spectra of the CC and ES interactions, pdfs were created for $T_{\rm eff}$ intervals ranging from 5.5 MeV to 13.5 MeV in 0.5-MeV steps. For $T_{\rm eff}$ values between 13.5 and 20 MeV, a single bin was used.

The extended maximum-likelihood analysis for the total data set from the second phase of SNO yielded 2176 $\pm$ 78 CC, 279 $\pm$ 26 ES, 2010 $\pm$ 85 NC, and 128 $\pm$ 42 external-source neutron events. There were also 125.4 internal neutron events and 3.5 internal gamma-ray events.

8.2.3. Results from phase two. The neutrino fluxes derived from the fitted CC, ES, and NC events, where the electron energy spectrum was unconstrained, are (in units of 10^6 cm^{-2} s^{-1})

$$\begin{aligned}\phi_{\rm CC} &= 1.68^{+0.06}_{-0.06}\,({\rm stat.})^{+0.08}_{-0.09}\,({\rm syst.}),\\ \phi_{\rm ES} &= 2.35^{+0.22}_{-0.22}\,({\rm stat.})^{+0.15}_{-0.15}\,({\rm syst.}), \quad \text{and}\\ \phi_{\rm NC} &= 4.94^{+0.21}_{-0.21}\,({\rm stat.})^{+0.38}_{-0.34}\,({\rm syst.}),\end{aligned}$$

and the ratio of the ^{8}B neutrino flux measured with the CC and NC reactions is

$$\frac{\phi_{\rm CC}}{\phi_{\rm NC}} = 0.340^{+0.023}_{-0.023}\,({\rm stat.})^{+0.029}_{-0.031}\,({\rm syst.}).$$

The quoted CC and ES fluxes are the equivalent fluxes of ^{8}B electron neutrinos, assuming an undistorted ^{8}B energy spectral shape (64) that would produce the same CC and ES event rates above the analysis threshold of $T_{\rm eff} = 5.5$ MeV. (Solar *hep* neutrinos could also be present in the measured fluxes; the SSM contribution would be 0.5%.)

A day-night analysis of the data was performed, and the measured values for the asymmetry ratio A from a shape-unconstrained signal extraction were $A_{CC} = -0.056 \pm 0.091$, $A_{NC} = 0.042 \pm 0.112$, and $A_{ES} = 0.146 \pm 0.201$, where the statistical and systematic errors have been combined in quadrature. No significant asymmetries were observed. A detailed discussion of the day-night analysis and results is given in Reference 60.

The observation of a substantially suppressed ν_e flux with the CC reaction compared to the total active flux measured by the NC reaction, provided clear evidence for neutrino flavor change that can be analyzed in terms of neutrino oscillations. The evidence is in very good agreement with the CC–ES comparison obtained in Phase One. A two-flavor, active neutrino oscillation model was used. This is a good approximation when θ_{13} is small.

The $T_{\rm eff}$ spectrum with statistical uncertainties for the data from the second phase of SNO is shown in **Figure 10*a***. Included are Monte Carlo spectra for neutron, CC, ES, and external-source neutron distributions. This spectrum is very similar to that predicted in 1987 in the SNO proposal (shown in **Figure 4**).

The best-fit parameters for a global oscillation analysis of the total data from the second phase of SNO, including solar neutrino and KamLAND reactor neutrino data, are $\Delta m^2 = 8.0^{+0.4}_{-0.3} \times 10^{-5}$ eV^2 and $\theta = 33.9^{+1.6}_{-1.6}{}^\circ$, where the errors reflect marginalized 1σ ranges. The predicted CC electron energy spectrum based on these best-fit parameters is compared to the measured CC spectrum in **Figure 10*b***.

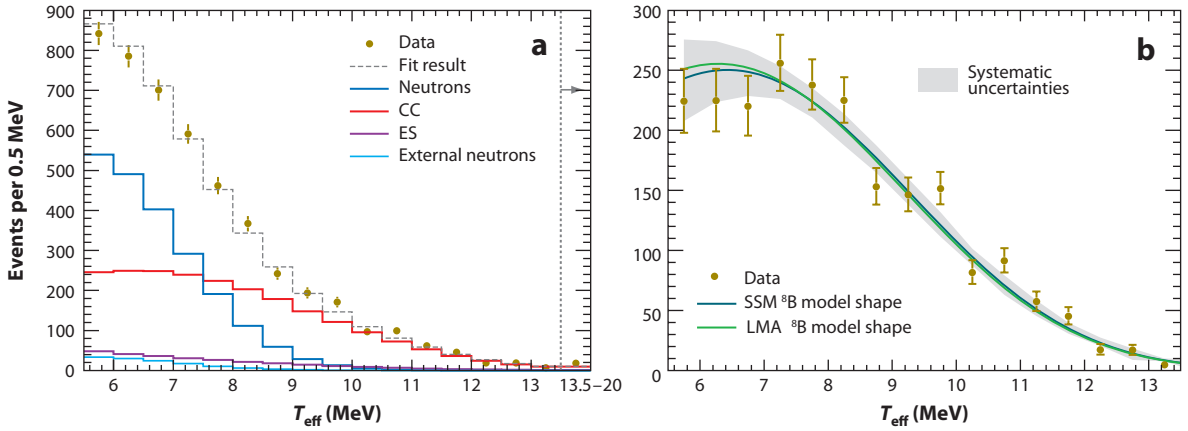

Figure 10

(*a*) Data T_{eff} spectrum with statistical uncertainties. Included are Monte Carlo (MC) spectra for neutron (*dark blue line*), charged-current (CC; *red line*), elastic scattering (ES; *purple line*), and external-source neutron (*light blue line*) distributions. Note that an undistorted ^{8}B spectral shape has been assumed and that each MC contribution has been normalized to the number of corresponding fit events measured by the energy-constrained signal. (*b*) Extracted CC T_{eff} spectrum compared to that predicted with the best-fit large mixing angle (LMA; *green line*) parameters. Only statistical uncertainties are shown in the data spectrum. The band in the LMA-predicted spectrum represents the 1σ uncertainty determined from detector systematic uncertainties. The predicted spectrum is normalized to the same number of counts as the data spectrum. Note that the data points, especially the first three points, are statistically correlated and also have correlated systematics (indicated by the error band). Abbreviation: SSM, Standard Solar Model.

The neutrino energy spectrum derived from the CC reaction is consistent with both the expected spectrum, assuming an undistorted ^{8}B shape, and the predicted spectrum, which corresponds to the best-fit LMA parameters for a global oscillation analysis that includes solar neutrino and KamLAND reactor neutrino data. Within uncertainties, no significant day-night asymmetries were observed, as was expected for the best-fit LMA solution. These data provided further confirmation of flavor change for solar neutrinos and for the oscillation of massive neutrinos as the dominant flavor change mechanism. The total flux of all active neutrino types for ^{8}B solar neutrinos is in agreement with solar model calculations (65, 66). The observation of the MSW effect in the Sun enables the relative size of m_1 and m_2 to be determined. With the usual convention, m_1, the mass eigenstate with the largest electron neutrino component, is found to be smaller than m_2. The angle θ_{12} is found to be less than the maximal value of 45° by more than five standard deviations, thereby providing significant restrictions on models for neutrino mixing.

8.3. Phase Three: Neutral-Current Detection Array

The extraction of the three neutrino-interaction signals from SNO with heavy water alone or with added dissolved salt requires a decomposition of the Cherenkov light signals into the three components on a statistical basis. Each signal has a characteristic isotropy and dependence on radius, angle with respect to the Sun's position, and energy. However, it is also possible to detect the NC disintegration of deuterium directly through use of neutron-sensitive proportional counters. This different approach breaks correlations that are present in the Cherenkov light signals and also provides a check on possible systematic effects.

Upon completion of the salt phase, the salt was removed by reverse osmosis and ion exchange, and a month's worth of data was taken to confirm that the detector and water clarity had returned to Phase One conditions. For Phase Three, an array of proportional counters filled with an 85:15

partial pressure mixture of ^{3}He and CF_4 was deployed in the heavy water to detect neutrons. A total of 40 strings of proportional counters were attached to anchor points on the inner surface of the vessel on a 1-m-square grid. The strings, laser-welded assemblies of individual counters 2 to 3 m in length, were 9 to 11 m long. Four strings contained ^{4}He instead of ^{3}He for assessment of backgrounds. A description of the design and deployment of this NCD array can be found in Reference 34. The results obtained from SNO's third phase are given in Reference 67.

8.3.1. Data. Data were acquired between November 27, 2004 and November 28, 2006 with the NCD array, for a total live time of 385.17 days. Diverse calibrations were also carried out to help track the performance and stability of both the PMT and the NCD systems as well as to aid in analysis. Calibration sources were deployed on two orthogonal planes bisecting the NCD array. A variety of sources were used: (*a*) two ^{252}Cf neutron sources, one of which was of precisely determined strength (60), (*b*) an ^{241}AmBe neutron source, (*c*) the ^{16}N source [the 6.13-MeV gammas from this source are the primary calibration of the PMT energy scale (49)], (*d*) the ^{8}Li source for calibration of event reconstruction and tests of instrumental cuts, (*e*) encapsulated Th and dissolved ^{222}Rn sources for background calibration, and (*f*) two ^{24}Na sources. Neutron-activated NaCl, precisely standardized by gamma counting, was dissolved in the heavy water in October 2005 and October 2006. The 2.754-MeV gammas photodisintegrated deuterium and created a source of neutrons that, like the neutrons produced by neutrino interactions, were nearly uniform and homogeneous. Small corrections were applied for edge effects at the vessel wall, and there was an uncertainty that arose from possible lack of mixing homogeneity. These sources were the primary calibration of NCD neutron efficiency. In addition, optical and electronic calibrations with pulser signals were carried out regularly on both the PMTs and the NCD array.

8.3.2. Analysis procedure. The extraction of the NC signal rate from the NCD array data began with the selection of good runs: generally, runs that are at least 30 minutes in duration and that have no abnormalities. As in the other phases, a blind analysis procedure was used. A total of 1834 neutrino runs were selected for the blind data, and another 121 were chosen as an open data set. Six of the ^{3}He strings were rejected from the final data because of mechanical and electrical problems. One string contained a counter that had leaked into the interspace between counters (but not into the heavy water), resulting in gain drift. Two strings had intermittent connections to their cables, and two others had an excess of low-amplitude events, possibly caused by an intermittent connection. Finally, one string exhibited fluctuating gain.

The PMT and NCD data contained instrumental or irrelevant events that were removed by a set of algorithms and cuts. For the PMT data, the cuts are as described in Reference 53, with some minor revisions. For the NCD data, the cuts are as described in Reference 34.

The remaining events consisted of neutrons, alpha particles, and possibly a low-energy component similar to that seen in the two strings, which had an excess of low-amplitude events. The alpha spectrum shape was simulated numerically in a detailed model of the physics and electronics responsible for the ionization profiles registered in the digitizers. Neutron spectra were also simulated, which confirmed the accuracy of the approach, but spectra taken from ^{24}Na runs were used to fit the neutron contribution to the spectrum from neutrino runs. **Figure 11** shows the results of the simulation.

Given the improvements to the calibration data analysis and the increased high voltage on the PMT array, the introduction of the NCD array did not significantly increase the position- or energy-reconstruction uncertainties from previous phases. A normalization for the

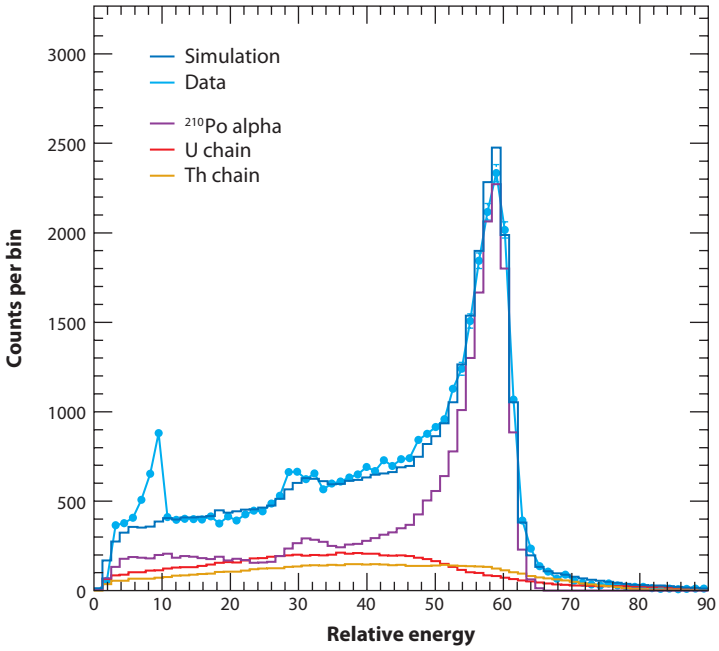

Figure 11

Comparison between a simulation of the neutral-current detection (NCD) alpha spectrum and the blind data (a fraction of the neutrino data plus some muon-produced neutrons). The peak near channel 10 is the neutron-capture peak at 764 keV, and the peak near channel 60 is dominated by the 5.3-MeV ^{210}Po alpha decay. The simulation is the curve (*dark blue*), consisting of the sum of the Th chain (*orange; lowest curve at channel 30*), the U chain (*red*), and the ^{210}Po alpha activities (*purple*), fitted to the data. The U and Th activities have exponential depth profiles in the Ni wall of the NCDs determined from fits to individual string data. The common scale depth for ^{210}Po is 0.1 μm.

photon-detection efficiency based on ^{16}N calibration data and Monte Carlo simulations was used to set the absolute energy scale with an uncertainty of 1.1%.

A table summarizing the neutron and Cherenkov light backgrounds in Phase Three can be found in Reference 67. Low levels of ^{214}Bi and ^{208}Tl present in the heavy and light water, NCD counters, and cables can create both free neutrons from deuteron photodisintegration and low-energy Cherenkov events from beta-gamma decays. The techniques (46–48, 55) described in Section 6.5 were used to determine these backgrounds in the water. For the NCD array, results from the in situ and ex situ methods gave comprehensive information about the isotopic composition and physical distribution of the activity and yielded the neutron background with an uncertainty of 1.5% of the NC signal.

The presence of neutrons from the acrylic vessel and light water had been noted in Phases One and Two (60, 63). Measurements, with Si counters, of alpha radioactivity on the inner surface of the acrylic vessel neck, below the normal waterline before and after the NCD phase, were consistent with those from the salt phase. Thus, the neutron contribution caused by ^{17,18}O(α, n) and ^{13}C(α, n) at the vessel wall was taken to be the same as for the salt phase. An additional contribution from photodisintegration caused by gammas passing through the vessel wall was determined from the measured ^{214}Bi and ^{208}Tl concentrations in the light water.

Backgrounds from Cherenkov events inside and outside the fiducial volume were estimated using calibration source data, measured activities, Monte Carlo calculations, and controlled injections

of Rn into the detector. These backgrounds were found to be small within the fiducial volume and above the analysis threshold of 6.0 MeV effective electron kinetic energy; they were included as an additional uncertainty on the flux measurements. In the previous phases, isotropic acrylic vessel background events had been identified and could be limited to 0.3 remaining isotropic background events (at 68% confidence) after data reduction for the NCD phase.

Blindness constraints were removed after all analysis procedures, parameters, and backgrounds were finalized. As described in Reference 67, some minor errors were discovered and corrected after "box opening". A simultaneous fit was made for the number of NC events detected by the NCDs; the numbers of NC, CC, and ES events detected by the PMTs; and the numbers of background events of various types. A Markov-chain Monte Carlo method was employed to make the fit; this method also allowed nuisance parameters (systematics) weighted by external constraints to vary in the fit. The NCD event energy spectrum was fit in the 0.4–1.4-MeV range with an alpha background distribution, a neutron calibration spectrum from ^{24}Na data, and two instrumental background event distributions. The PMT events were fit in reconstructed energy, the cosine of the event direction relative to the vector from the Sun ($\cos\theta_{\rm Sun}$), and the reconstructed radial position.

The spectral distributions of the ES and CC events were not constrained to the ^{8}B shape, but rather were extracted from the data. Fits to the data yielded the following numbers of events: 983^{+77}_{-76} NC (NCD array), 267^{+24}_{-22} NC (PMT array), 1867^{+91}_{-101} CC, and 171^{+24}_{-22} ES, with 185^{+25}_{-22} and 77^{+12}_{-10} neutron background events in the NCD and PMT arrays, respectively. Additionally, the total NCD array background fits including alphas and the two instrumental components yielded 6127 ± 101 events.

8.3.3. Results from phase three. Assuming the ^{8}B neutrino spectrum from Reference 68, the equivalent neutrino fluxes derived from the fitted CC, ES, and NC events are (in units of 10^6 cm^{-2} s^{-1})

$$\begin{aligned}\phi_{\rm CC} &= 1.67^{+0.05}_{-0.04}\,(\text{stat.})^{+0.07}_{-0.08}\,(\text{syst.}),\\ \phi_{\rm ES} &= 1.77^{+0.24}_{-0.21}\,(\text{stat.})^{+0.09}_{-0.10}\,(\text{syst.}), \quad \text{and}\\ \phi_{\rm NC} &= 5.54^{+0.33}_{-0.31}\,(\text{stat.})^{+0.36}_{-0.34}\,(\text{syst.}),\end{aligned}$$

and the ratio of the ^{8}B neutrino flux measured with the CC and NC reactions is

$$\frac{\phi_{\rm CC}}{\phi_{\rm NC}} = 0.301 \pm 0.033\,(\text{total}).$$

Neutrinos from *hep* capture may also be present in the measured fluxes; the SSM contribution would be 0.5%.

The ES flux presented here is 2.2σ lower than that found by Super-Kamiokande-I (69) and is apparently a downward statistical fluctuation, as evidenced in the shortfall of signals near $\cos\theta_{\rm Sun} = 1$ in two isolated energy bins. The ^{8}B spectral shape used here (68) differs from that used in previous SNO results (64). The CC, ES, and NC flux results are in agreement [$p = 32.8\%$ (70)] with the NC flux result of the D_2O phase (55) and with the fluxes from the salt phase (60).

The fluxes, combined with day and night energy spectra from the pure D_2O and salt phases (58, 60), place constraints on neutrino flavor mixing parameters. Two-flavor active neutrino oscillation models are used to predict the CC, NC, and ES rates in SNO. A combined χ^2 fit to SNO D_2O-, salt-, and NCD-phase data yields the allowed regions in Δm^2 and $\tan^2\theta$ shown in **Figure 12*a***. Data from a global analysis of all solar neutrino data, including Borexino (71) and Super-Kamiokande-I (69), as well as the 2881-tonne-year KamLAND reactor antineutrino results (29), yielded the

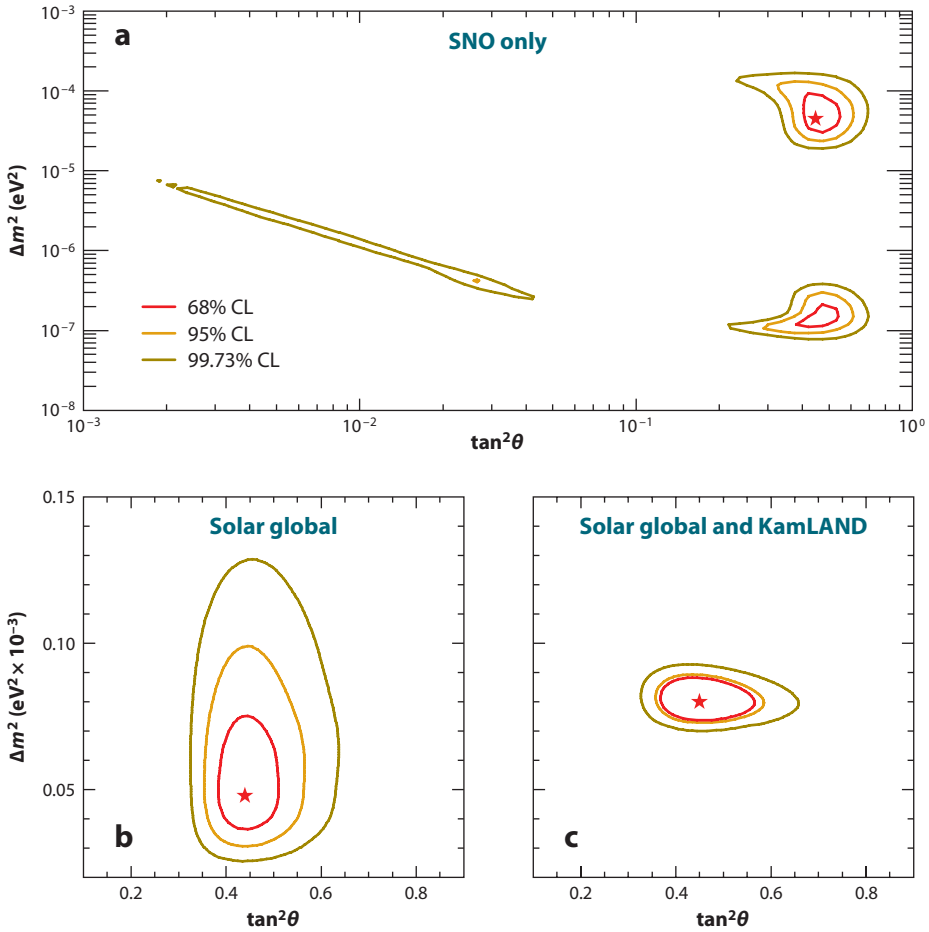

Figure 12

Neutrino-oscillation contours. (*a*) SNO only: D_2O- and salt-phase day and night spectra and neutral-current detection–phase fluxes. The best-fit point is $\Delta m^2 = 4.57 \times 10^{-5}$ eV^2, $\tan^2\theta = 0.447$, $f_B = 0.900$, with χ^2 per degree of freedom = 73.77/72. (*b*) Solar global: SNO, SK, Cl, Ga, and Borexino. The best-fit point is $\Delta m^2 = 4.90 \times 10^{-5}$ eV^2, $\tan^2\theta = 0.437$, $f_B = 0.916$. (*c*) Solar global and KamLAND. The best-fit point is $\Delta m^2 = 7.59 \times 10^{-5}$ eV^2, $\tan^2\theta = 0.468$, $f_B = 0.864$.

allowed regions presented in **Figure 12*b*,*c***. Here, we treat the three phases of SNO as separate experiments, with correlations taken into account. However, a three-phase unified analysis is in progress. The best-fit point to the solar global plus KamLAND data yields $\Delta m^2 = 7.59^{+0.19}_{-0.21} \times 10^{-5}$ eV^2 and $\theta = 34.4^{+1.3}_{-1.2}{}^\circ$, where the errors reflect marginalized 1σ ranges. In our analyses, the ratio f_B of the total ^{8}B flux to the SSM (65) value was a free parameter, whereas the total *hep* flux was fixed at 7.93×10^3 cm^{-2} s^{-1} (72).

The third and final phase of SNO enabled a determination of the total flux of active ^{8}B neutrinos from the Sun that was independent of the methods used in the previous phases. There is generally good agreement among the three phases, consistent with the absence of unexpected systematic errors. The flux is in agreement with SSM calculations, and the uncertainty in θ is reduced.

9. OTHER PHYSICS

SNO provided opportunities to investigate several other interesting physical processes. The detector's large target mass, coupled with its very low radioactivity, meant that stringent limits could be set on a number of hypothesized or rare processes. In this section, we summarize the findings and briefly describe the ongoing analysis of the SNO data for such events.

9.1. Supernova and Relic Neutrinos

A supernova at the middle of our galaxy could provide a burst of up to 1000 neutrino interactions lasting for only a few seconds. At SNO, a system was developed to provide a rapid analysis of such an event that might allow astronomers to receive early warning prior to the onset of the light curve for a supernova (which takes place as much as several hours after the initial neutrino burst). SNO also participated in the SuperNova Early Warning System project, wherein a central computer receiving possible signals from several international neutrino experiments could, in the event of a coincidence, alert the astrophysical community. During the course of the SNO experiment, no such event was seen.

SNO also searched (73) for the diffuse supernova neutrino background (DSNB) using data collected during its first operational phase, with an exposure of 0.65 ktonne-years. No events were observed in the effective electron energy range of 21 MeV $< T_{\rm eff} <$ 35 MeV (see **Figure 13*a***) and, consequently, an upper limit on the ν_e component of the DSNB flux in the neutrino energy range of 22.9 MeV $< E <$ 36.9 MeV of 70 cm^{-2} s^{-1} was inferred at the 90% confidence level.

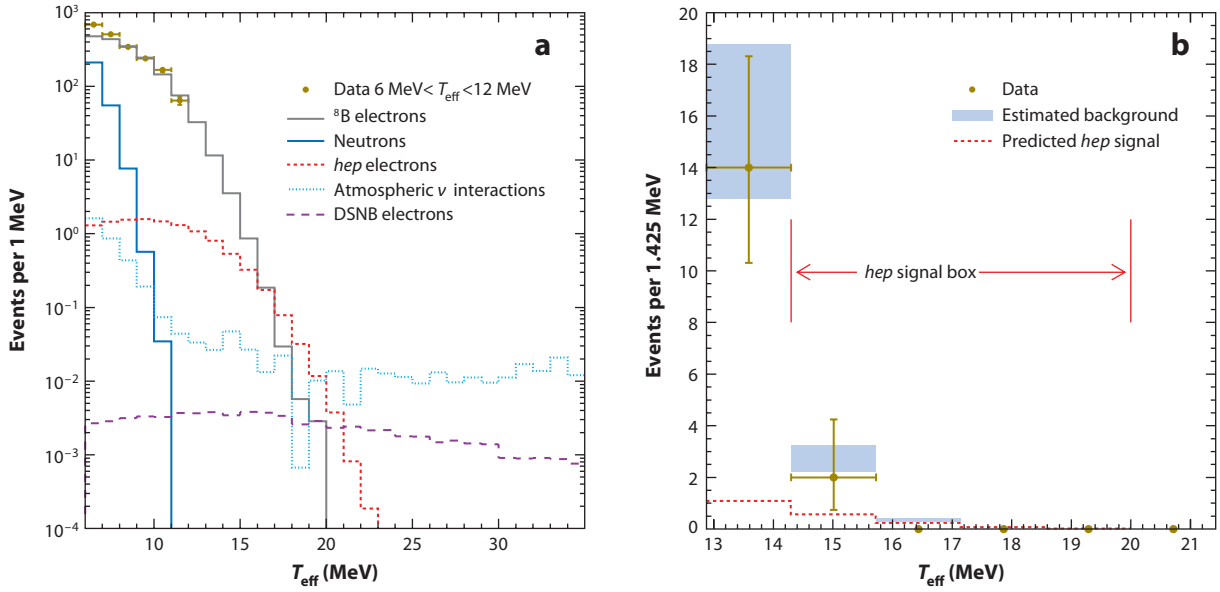

Figure 13

(*a*) The simulated effective electron kinetic energy spectra of the signals and backgrounds of interest in the *hep* (^{3}He + $p \rightarrow$ ^{4}He + e^+ + ν_e) and diffuse supernova neutrino background (DSNB) analyses. Also shown are the data in the range 6 MeV $< T_{\rm eff} <$ 12 MeV, which are used to normalize the ^{8}B electron and neutron distributions. (*b*) The distribution of events in the region of the ^{8}B end point. There are two events in the *hep* signal box 14.3 $< T_{\rm eff} <$ 20 MeV. Also shown are the estimated number of background events, including the systematic uncertainty, and the Standard Solar Model prediction for the *hep* signal.

This result is an improvement of two orders of magnitude over the previous ν_e limit (74). The same data were used to look for evidence of *hep* neutrinos in the Sun.

9.2. Solar *hep* Neutrinos

The simulated effective electron kinetic energy spectra of the signals and backgrounds of interest in the *hep* and DSNB analyses are shown in **Figure 13*a***, and the distribution of events in the region of the ^{8}B end point is shown in **Figure 13*b*** (73). There are two events in the *hep* signal box 14.3 MeV $< T_{\rm eff} <$ 20 MeV, where 3.1 background events are expected. After accounting for neutrino oscillations, an upper limit of 2.3×10^4 cm^{-2} s^{-1} at the 90% confidence level was inferred on the integral total flux of *hep* neutrinos. This measurement represents a 6.5-fold improvement over the previous best limit on the *hep* neutrino flux, measured with the Super-Kamiokande detector. It is consistent with the SSM. A model-independent limit on the integral *hep* ν_e flux, with no assumptions about neutrino oscillations, is set at 3.1×10^4 cm^{-2} s^{-1}.

9.3. Constraints on Nucleon Decay via "Invisible" Modes

Experimental signatures of the grand unification of the electroweak and strong interactions have been sought with increasing sensitivity for the past 25 years. Much effort has gone into identifying specific decay modes of free protons and bound nucleons as signatures of grand unification, but to date no signal has been observed. Decay modes that are more unusual than those typically explored cannot, however, be ruled out. A recent paper has even suggested a model in which $n \rightarrow 3\nu$ becomes the dominant mode (75).

Data from Phases One and Two of SNO have been used to constrain the lifetime for nucleon decay to "invisible" modes, such as $n \rightarrow 3\nu$. The analysis (76) was based on a search for gamma rays from the de-excitation of the residual nucleus that would result from the disappearance of either a proton or a neutron from ^{16}O. The gamma rays from the nucleon-decay signal were detected with similar efficiencies in Phases One and Two, whereas neutrons produced by ^{8}B solar neutrinos were detected with very different efficiencies. Comparing the number of neutron-like signals found in Phase One and in Phase Two allowed a limit on the number of gamma rays from the de-excitation of the residual nucleus that would result from the disappearance of either a proton or a neutron from ^{16}O to be set.

A limit of $\tau_{\rm inv} > 2 \times 10^{29}$ years was obtained at 90% confidence for either neutron- or proton-decay modes. This limit is approximately an order of magnitude more stringent than previous constraints on invisible proton-decay modes and 400 times more stringent than similar neutron-decay modes. [In 2006, the KamLAND experiment reported (77) improved limits of $\tau(n \rightarrow \text{inv.}) > 5.8 \times 10^{29}$ years and $\tau(nn \rightarrow \text{inv.}) > 1.4 \times 10^{30}$ years at 90% confidence.]

A search for evidence for neutron-antineutron oscillation is currently under way. The signal for neutrons in deuterium would be $\bar{n}p$ annihilation at rest, and a possible channel to look for would be $2\pi^+ + \pi^- + \pi^0$.

9.4. A Search for Periodicities in the ^{8}B Solar Neutrino Flux

A search (78) has been made for sinusoidal periodic variations in the ^{8}B solar neutrino flux using data collected by SNO over a four-year interval. The variation at a period of one year is consistent with modulation of the ^{8}B neutrino flux by the Earth's orbital eccentricity: A fit yielded $\varepsilon = 0.0143 \pm 0.0086$, in good agreement with the known value of 0.0167. Neither an unbinned maximum-likelihood analysis nor a Lomb-Scargle periodogram analysis has revealed any other significant

sinusoidal periodicities with periods between one day and ten years. Searches for time dependence in astrophysical neutrino sources, using a Rayleigh Power test, and for "no-trigger" neutrino bursts, such as from an optically occluded supernova, are under way.

9.5. Antineutrino and Fractionally Charged Particle Searches

Upper limits on solar $\bar{\nu}_e$ fluxes have been set (79) based on the $\bar{\nu}_e$ CC reaction on deuterium, which produces a positron and two neutrons in coincidence. This distinctive signature allows a search with very low background for $\bar{\nu}_e$ s from the Sun and from other potential sources. For an energy-independent $\nu_e \rightarrow \bar{\nu}_e$ conversion mechanism, the integral limit on the flux of solar $\bar{\nu}_e$ s in the energy range from 4 to 14.8 MeV has been found to be $\bar{\nu}_e < 3.4 \times 10^4$ cm^{-2} s^{-2} (at 90% confidence), which corresponds to 0.81% of the SSM ^{8}B ν_e flux of 5.05×10^6 cm^{-2} s^{-1} and is consistent with the more sensitive limit from KamLAND in the 8.3–14.8-MeV range of 3.7×10^2 cm^{-2} s^{-1} (at 90% confidence).

The great depth of SNO (5800 m.w.e.) reduces the background neutron rate from muon-induced reactions. Any fractionally charged particles passing through SNO would give less Cherenkov light per unit path length, and searches for this signature will be performed in the future.

9.6. The Cosmic Ray– and Neutrino-Induced Muon Flux at the Sudbury Neutrino Observatory

For muon zenith angles larger than 66°, the primary muon flux detected at SNO falls below the flux of secondary muons produced by the interaction in the rock of neutrinos created by the decay of muons and pions. The direction of these secondary muons is not very different from that of the neutrinos that created them. Neutrinos incident from below the horizon have traveled distances as great as the diameter of the Earth, whereas those coming from above the horizon have traveled relatively short distances. SNO muon data above and below the horizon (79a) are consistent with current phenomenological models for downward fluxes of atmospheric muons versus depth and provide a measurement of atmospheric neutrino oscillations in agreement with (though less accurate than) previous measurements of such oscillations (81, 82).

10. CONCLUSIONS

The SNO experiment operated from November 1999 through November 2006, recording solar neutrino data via three reactions (ES on electrons, and CC and NC interactions on deuterium) in three configurations or phases (heavy water alone, heavy water with dissolved salt, and heavy water with neutron-detecting proportional counters deployed). The ES data agree with the much higher statistics data from Super-Kamiokande (69). The NC rate yields the flux of all active neutrino flavors above 2.2 MeV, a result in excellent agreement with the predictions of standard solar models such as that developed by Bahcall et al. (65). The extraordinary accomplishments of astrophysical theory can be judged by the dependence of the ^{8}B flux on the twenty-fourth power of the central temperature of the Sun (80), implying that the temperature has been correctly predicted to ~1% accuracy despite decades of contraindication.

The three reactions observed at SNO permit an overdetermined fit to the fluxes of electron and nonelectron flavors, and the agreement is good. This evidence for neutrino flavor conversion and appearance is consistent with the theoretical picture of oscillations between two mass eigenstates and matter enhancement by the MSW effect. The electron neutrino has been found to be a state

of mixed mass like the mu and tau neutrinos were shown to be from an analysis of atmospheric neutrino data (81, 82). The linkage of the three mass eigenstates via oscillation leads to upper and lower bounds (83) on the sum of neutrino masses. Neutrino mass requires revision of the Standard Model of particles and fields. The increasingly accurate results obtained from the SNO experiment are helping to provide strong constraints on neutrino properties and to guide theoretical work seeking to define the required revision.

Further analysis of the extant SNO data continues. A concordant set of fluxes, spectra, and day-night asymmetry from the three phases taken together will be extracted, accounting for correlations. With many refinements to the analysis methods, the threshold for the first two phases will be lowered below the current 5.0-MeV value. At present, the practical approach for combining the results of the three phases is to treat them as independent both statistically and systematically, a very good approximation. SNO is undertaking a three-neutrino analysis in parallel with the improvements mentioned. Solar neutrinos can provide information about the third mixing angle, θ_{13}, because θ_{12} and θ_{13} phenomena have different energy dependences owing to matter enhancement in the Sun for θ_{12} above a certain energy. Comprehensive three-neutrino analyses incorporating the results already published have been reported by Fogli et al. (84) and Schwetz et al. (85).

SNO has almost completed its task, with results that have proven to be exciting and significant to both physics and astrophysics. The study of solar neutrinos is not yet complete, but several ingenious new experiments have been proposed to explore the spectrum below 5 MeV with precision and detail.

DISCLOSURE STATEMENT

The authors are not aware of any affiliations, memberships, funding, or financial holdings that might be perceived as affecting the objectivity of this review.

ACKNOWLEDGMENTS

We cannot hope to do justice to the tremendous amount of work that has gone into the SNO project by our colleagues over many years. This work is best understood through reading the detailed SNO papers cited in this article, and our colleagues' names are contained in the extensive author lists for those papers. The SNO collaboration is indebted to the financial and other support that it has received from many sources [Canada: NSERC, Industry Canada, NRC, Northern Ontario Heritage Fund, Vale Inco, AECL, Ontario Power Generation, HPCVL, CFI, CRC, Westgrid; United States: Department of Energy, NERSC PDSF; United Kingdom: STFC (formerly PPARC); Portugal: FCT]. We are also indebted to the dedicated and talented technical staff on-site at Sudbury and at the many institutions across the project for their important contributions.

LITERATURE CITED

1. Davis R, Evans JC, Cleveland BT. *AIP Conf. Proc.* 52:17–27 (1979)
2. Bahcall JN, Pinsonneault MH, Basu S. *Astrophys. J.* 555:990 (2001)
3. Brun S, Turck-Chieze AS, Zahn JP. *Astrophys. J.* 525:1032 (1999)
4. Chen HH. *Phys. Rev. Lett.* 55:1534 (1985)
5. Bahcall JN, Pena-Garay C. *N. J. Phys.* 6:63 (2004)
6. Bahcall JN, Pinsonneault HM. *Phys. Rev. Lett.* 92:121301 (2004)
7. Davis R. *Phys. Rev. Lett.* 20:1205 (1968)
8. Bahcall JN. *Nucl. Phys. B* 118:77 (2003)

9. Bahcall JN, et al. *Astrophys. J.* 184:1 (1973)
10. Hirata S, et al. *Phys. Rev. Lett.* 65:1297 (1990)
11. Bahcall JN. *Astrophys. J.* 467:475 (1996)
12. Abdurashitov JN, et al. *Phys. Lett.* B328:234 (1994)
13. Anselmann P, et al. *Phys. Lett.* B342:440 (1995)
14. Hata N, Langacker P. *Phys. Rev. D* 56:6107 (1997)
15. Heeger KM, Robertson RGH. *Phys. Rev. Lett.* 77:3720 (1996)
16. Pontecorvo B. *Zh. Eksp. Teor. Fiz.* 53:1717 (1967)
17. Gribov V, Pontecorvo B. *Phys. Lett.* B28:493 (1969)
18. Perl ML, et al. *Phys. Rev. Lett.* 35:1489 (1975)
19. Maki Z, Nakagawa N, Sakata S. *Prog. Theor. Phys.* 28:870 (1962)
20. Amsler C, et al. (Part. Data Group) *Phys. Lett.* B667:1 (2008)
21. Wolfenstein L. *Phys. Rev. D* 17:2369 (1978)
22. Langacker P, Liu J. *Phys. Rev. D* 46:4140 (1992)
23. Mikheyev SP, Smirnov AY. *Sov. J. Nucl. Phys.* 42:913 (1985)
24. Glashow SL, Krauss LM. *Phys. Lett.* B190:199 (1987)
25. Balantekin AB, Loreti F. *Phys. Rev. D* 45:1059 (1992)
26. Abazov AI, et al. *Phys. Rev. Lett.* 67:3332 (1991)
27. Cribier M, Hampel W, Rich J, Vignaud D. *Phys. Lett.* B182:89 (1986)
28. Baltz AJ, Weneser J. *Phys. Rev. D* 35:528 (1987)
29. Abe S, et al. (KamLAND Collab.) *Phys. Rev. Lett.* 100:221803 (2008)
30. Beacom JF, Bell NF. *Phys. Rev. D* 65:113009 (2002)
31. Lim C-S, Marciano WJ. *Phys. Rev. D* 37:1368 (1988)
32. Valdiviesso GdA, Guzzo MM, de Holanda PC. arXiv:0811.2128 (2008)
33. Ewan GT, et al. (SNO Collab.) *Propos. SNO-8712* (1987)
34. Amsbaugh JF, et al. *Nucl. Instrum. Methods A* 579:1054 (2007)
35. Davidson WF, et al. *Proc. Intl. Colloq. Baryon Nonconserv. (ICOBAN)* 84:273 (1984)
36. Chen HH. *AIP Conf. Proc.* 126:249 (1985)
37. Ewan GT, Davidson WF. *Phys. Can.* 61:339 (2005)
38. Sinclair D, et al. *Nuovo Cim.* C9:308 (1986)
39. Aardsma G, et al. *Phys. Lett.* B194:321 (1987)
40. Jagam P, Simpson JJ. *Nucl. Instrum. Methods A* 324:389 (1993)
41. Jillings CJ, et al. (SNO Collab.) *Nucl. Instrum. Methods A* 373:421 (1996)
42. Doucas G, et al. *Nucl. Instrum. Methods A* 370:579 (1996)
43. Heaton RK, et al. *Phys. Rev. C* 56:922 (1997)
44. Boger J, et al. (SNO Collab.) *Nucl. Instrum. Methods A* 449:172 (2000)
45. Howe MA, et al. *IEEE Trans. Nucl. Sci.* 51:878 (2004)
46. Andersen TC, et al. (SNO Collab.) *Nucl. Instrum. Methods A* 501:399 (2003)
47. Andersen TC, et al. (SNO Collab.) *Nucl. Instrum. Methods A* 501:386 (2003)
48. Blevis I, et al. *Nucl. Instrum. Methods A* 517:139 (2004)
49. Dragowsky MR, et al. *Nucl. Instrum. Methods A* 481:284 (2002)
50. Tagg NJ, et al. *Nucl. Instrum. Methods A* 489:178 (2002)
51. Moffat BA, et al. *Nucl. Instrum. Methods A* 554:225 (2005)
52. Brun R, et al. (ZEBRA Collab.) *CERN Program Libr. Q100/101* (1986)
53. Aharmim B, et al. (SNO Collab.) *Phys. Rev. C* 75:045502 (2007)
54. Ahmad QR, et al. (SNO Collab.) *Phys. Rev. Lett.* 87:071301 (2001)
55. Ahmad QR, et al. (SNO Collab.) *Phys. Rev. Lett.* 89:011301 (2002)
56. Fukuda S, et al. *Phys. Rev. Lett.* 86:5651 (2001)
57. Turck-Chieze S, et al. *Astrophys. J. Lett.* 5:555 (2001)
58. Ahmad QR, et al. (SNO Collab.) *Phys. Rev. Lett.* 89:011302 (2002)
59. Hata N, Langacker P. *Phys. Rev. D* 52:420 (1995)
60. Aharmim B, et al. (SNO Collab.) *Phys. Rev. C* 72:055502 (2005)

61. LaBranche H. *Time series analysis for the Cf source in Sudbury Neutrino Observatory. M.Sc. thesis.* Univ. Guelph (2003)
62. Nelson WR, Hirayama H, Rogers DWO. *SLAC Rep. 265* (1985)
63. Ahmed SN, et al. (SNO Collab.) *Phys. Rev. Lett.* 92:181301 (2004)
64. Ortiz CE, et al. *Phys. Rev. Lett.* 85:2909 (2000)
65. Bahcall JN, Serenelli AM, Basu S. *Astrophys. J.* 621:L85 (2005)
66. Turck-Chieze S, et al. *Phys. Rev. Lett.* 93:221102 (2004)
67. Aharmim B, et al. (SNO Collab.) *Phys. Rev. Lett.* 101:111301 (2008)
68. Winter WT, Freedman SJ, Rehm KE, Schiffer JP. *Phys. Rev. C* 73:025503 (2006)
69. Hosaka J, et al. (Super-Kamiokande Collab.) *Phys. Rev. D* 73:112001 (2006)
70. Valassi A. *Nucl. Instrum. Methods A* 500:391 (2003)
71. Borexino, Arpesella C, et al. *Phys. Rev. Lett.* 101:091302 (2008)
72. Bahcall JN, Serenelli AM, Basu S. *Astrophys. J. Suppl.* 165:400 (2006)
73. Aharmim B, et al. (SNO Collab.) *Astrophys. J.* 653:1545 (2006)
74. Aglietta M, et al. *Astropart. Phys.* 1:1 (1992)
75. Mohapatra RN, Perez-Lorenzana A. *Phys. Rev. D* 67:075015 (2003)
76. Ahmed SN, et al. (SNO Collab.) *Phys. Rev. Lett.* 92:102004 (2004)
77. Araki T, et al. *Phys. Rev. Lett.* 96:101802 (2006)
78. Aharmim B, et al. (SNO Collab.) *Phys. Rev. D* 72:052010 (2005)
79. Aharmim B, et al. (SNO Collab.) *Phys. Rev. D* 70:093014 (2004)

79a. Aharmim B, et al. (SNO Collab.) arXiv:0902.2776 (2009)

80. Bahcall JN, Ulmer A. *Phys. Rev. D* 53:4202 (1996)
81. Itow Y. (Super-Kamiokande Collab.) *J. Phys. Conf. Ser.* 120:052037 (2008)
82. Abe K, et al. (Super-Kamiokande Collab.) *Phys. Rev. D* 77:052001 (2008)
83. Robertson RGH. *J. Phys. Conf. Ser.* In press. arXiv:0807.4258 (2008)
84. Fogli GL, et al. *Phys. Rev. Lett.* 101:141801 (2008)
85. Schwetz T, Tortola M, Valle JWF. *N. J. Phys.* 10:113011 (2008)